Running title: Functional diversification in COPII gene families

COPII Sec23 proteins form isoform-specific ER exit sites with differential effects on polarized growth

Mingqin Chang[1,2,3], Shu-Zon Wu[1], Samantha E. Ryken[1], Jacquelyn E. O'Sullivan[4,5] and Magdalena Bezanilla[1]*

[1] Department of Biological Sciences, Dartmouth College, Hanover, NH 03755
[2] Plant Biology Graduate Program, University of Massachusetts Amherst, Amherst, MA 01002
[3] Current address: Department of Plant Sciences, University of California Davis, Davis, CA 95616
[4] Department of Biology, University of Massachusetts Amherst, Amherst, MA 01002
[5] Current address: Tufts School of Medicine, Boston, MA 02111

*Corresponding author
email: magdalena.bezanilla@dartmouth.edu

The author responsible for distribution of materials integral to the findings presented in this article in accordance with the policy described in the Instructions for Authors (www.plantcell.org) is: Magdalena Bezanilla (magdalena.bezanilla@dartmouth.edu).

Abstract

COPII, a coat of proteins that form vesicles on the ER, mediates vesicle traffic from the ER to the Golgi. In contrast to metazoans that have few genes encoding each COPII component, plants have expanded these gene families leading to the hypothesis that plant COPII has functionally diversified. Here, we analyzed the gene families encoding for the Sec23/24 heterodimer in the moss *Physcomitrium (Physcomitrella) patens*. In *P. patens*, *Sec23* and *Sec24* gene families are each comprised of seven genes. Silencing the Sec23/24 genes revealed isoform specific contributions to polarized growth, with the closely related *Sec23D/E* and *Sec24C/D* essential for protonemal development. Focusing on the *Sec23* gene family, we discovered that loss of Sec23D alters ER morphology, increases ER stress, inhibits trafficking to the Golgi and to the plasma membrane in tip growing protonemata. In contrast, the remaining five *Sec23* genes are dispensable for tip growth. While *Sec23A/B/C/F/G* do not quantitatively affect ER to Golgi trafficking in protonemata, they do contribute to secretion to the plasma membrane. Of the three highly expressed Sec23 isoforms in protonemata, Sec23G forms ER exit sites that are larger than Sec23B and Sec23D and do not overlap with Sec23D. Furthermore, ER exit sites labeled by Sec23B or Sec23G form in the absence of Sec23D. These data suggest that *Sec23D/E* form unique ER exit sites contributing to secretion that is essential for tip growing protonemata.

53 **Introduction**

54 Trafficking from the ER to the Golgi is mediated by the Coat Protein
55 complex II (COPII). COPII facilitates the formation of transport vesicles at ER exit
56 sites promoting the delivery of cargo, including transmembrane proteins, soluble
57 proteins and lipids, to *cis*-Golgi compartments (Brandizzi and Barlowe, 2013;
58 Barlowe and Helenius, 2016; Aridor, 2018; Hanna et al., 2018; Robinson et al.,
59 2015). The COPII coat comprises two layers of protein complexes. The inner
60 layer consists of a Sar1-Sec23-Sec24 lattice, while the outer layer is made up of
61 Sec31-Sec13 heterotetramers (Stagg et al., 2008; Whittle and Schwartz, 2010; Bi
62 et al., 2002; Fath et al., 2007). Sar1 is a small GTPase of the Ras super family that
63 is the master regulator of COPII vesicle biogenesis (Nakano and Muramatsu,
64 1989). Assembly of COPII coat is initiated by the conversion of Sar1-GDP to Sar1-
65 GTP, which is mediated by Sec12, a guanine nucleotide exchange factor (GEF)
66 that is an ER resident membrane protein (Barlowe and Schekman, 1993; Nakano
67 and Muramatsu, 1989). At the ER surface, activated Sar1 recruits the Sec23-
68 Sec24 heterodimer, which associates with the ER membrane as an "inner coat".
69 The Sar1-Sec23-Sec24-cargo "pre-budding" complex in turn recruits the Sec13-
70 Sec31 heterotetramer, referred to as an "outer coat" to the nascent bud (Aridor
71 et al., 1998; Salama et al., 1993). The polymerization of Sec13-Sec31
72 heterotetramers induces membrane curvature and completes vesicle biogenesis
73 (Fath et al., 2007; Stagg et al., 2006; Whittle and Schwartz, 2010).

74 Selective recruitment of cargos into COPII coated vesicles is driven by ER
75 export signals located on cytoplasmically exposed regions of cargo proteins
76 (Barlowe, 2003). ER export signals of most transmembrane cargo proteins are
77 thought to interact directly with the inner coat components of COPII. However,
78 some transmembrane and most soluble cargo proteins interact with COPII
79 components through ER-resident transmembrane adaptors or receptors
80 (Barlowe, 2003). Sec24 is the COPII component that has been implicated in
81 recognizing these various sorting signals (Mossessova et al., 2003; Nufer, 2003).
82 However, several studies suggested that Sec23 and Sar1 may also play roles in
83 cargo sorting by directly binding to the export signals (Aridor et al., 2001;
84 Mancias and Goldberg, 2007; Giraudo and Maccioni, 2003).

85 Based on the high sequence similarity among COPII paralogs, and cross-
86 species complementation studies (De Craene et al., 2014; Khoriaty et al., 2018), it
87 has been assumed that functions of COPII components are conserved across
88 eukaryotes. While components of the COPII coat are well studied in budding
89 yeast and mammalian cells, illustrating their molecular functions in plants has
90 been more challenging. Comparative genomic analyses revealed that gene
91 families encoding COPII components have undergone gene expansions in plants
92 with *Sec23* exhibiting the largest expansion (Aridor et al., 2001; Mancias and
93 Goldberg, 2007; Giraudo and Maccioni, 2003; Schlacht and Dacks, 2015). While
94 there are only one and two *Sec23* genes in *S. cerevisiae* and mammals (eg. mice
95 and humans) (Jensen and Schekman, 2011), respectively, there are seven in both
96 *P. patens* and *A. thaliana* (Brandizzi, 2018). Since Sec23 and its heterodimeric
97 partner Sec24 are implicated in cargo sorting, the larger *Sec23* gene family could
98 suggest that plants have more diverse sorting signals requiring specificity at the
99 level of the Sec23/Sec24 heterodimer. Consistent with this, in contrast to yeast,
100 which has a single gene for most COPII components, all other components of
101 COPII in plants are encoded by multiple genes, suggesting that cargo specificity
102 may translate to formation of distinct COPII complexes and vesicle populations.
103 Alternatively, larger gene families could simply indicate that plants have higher
104 functional redundancy in COPII encoded gene families.
105 Genetic studies in *A. thaliana* have demonstrated that loss of specific
106 COPII components caused developmental defects. A complete knockout of
107 AtSec24A was lethal (Faso et al., 2009; Nakano et al., 2009). However, a missense
108 point mutation in AtSec24A (R693K) resulted in ER morphology defects and
109 disruption of ER-Golgi integrity. Interestingly, these phenotypes could not be
110 rescued by either AtSec24B or AtSec24C (Faso et al., 2009; Nakano et al., 2009),
111 suggesting that AtSec24B and C are functionally distinct from AtSec24A. Even
112 though AtSec24B and AtSec24C did not rescue the *Atsec24a* missense mutant
113 and each were not important for plant viability, they were shown to influence the
114 development of reproductive cells (Tanaka et al., 2013). Functional
115 diversification was also suggested by analysis of AtSec16 mutants in which
116 storage protein precursors were accumulated abnormally in *Atsec16a* null
117 mutants, but not in *Atsec16b* null mutants (Takagi et al., 2013).

118 While *P. patens* and *A. thaliana* have similar numbers of genes encoding
119 COPII components, moss has several attributes that make it particularly suited to
120 study COPII function. *P. patens* juvenile tissues are haploid and comprise
121 multiple tissue types that establish the plant body. Protonemal tissue, which
122 emerges from the spore and is also readily propagated vegetatively by tissue
123 homogenization, is composed of tip-growing cells constituting a two-
124 dimensional filamentous network. The predictable patterns of growth and cell
125 division provide an easily tractable system for analysis of mutant phenotypes. As
126 a single-cell-layer, protonemal tissue also enables high-resolution microscopy of
127 endogenously tagged fluorescent proteins in live cells (Rensing et al., 2020). In
128 addition to amenable tissue morphology and haploid lifestyle, *P. patens* is
129 amenable to transient RNA interference for rapid identification of gene function
130 and exhibits high rates of CRISPR Cas9-mediated genome editing (Rensing et al.,
131 2020; Mallett et al., 2019). Here, we utilized these molecular genetic and live-cell
132 imaging tools to systematically characterize the *Sec23* and *Sec24* gene families.
133 Analysis of mutant phenotypes revealed a high degree of functional specificity
134 among Sec23 and Sec24 isoforms. Focusing on the *Sec23* gene family, we
135 discovered that Sec23 isoforms differentially influence ER to Golgi trafficking,
136 and secretion to the plasma membrane as well as the size of presumptive ER exit
137 sites.
138
139 **Results**
140 ***Sec23 and Sec24 isoforms differentially affect tip growth***
141 *P. patens* has seven *Sec23* and seven *Sec24* genes. Based on sequence
142 similarity, we found that there are four subclasses of *Sec23* and *Sec24* genes and
143 in both cases six of the seven genes exist in closely related pairs (Fig 1A, B). For
144 *Sec23*, with the exception of *Sec23A*, at least one member of each subclass is
145 highly expressed in protonemal cells (Fig 1A). For *Sec24*, we found that one of
146 the seven *Sec24* genes (*Sec24E)* was not expressed in protonemata (Fig1B). Of
147 the remaining six genes, *Sec24D* exhibited the lowest expression while the other
148 five Sec24 genes were expressed at similar levels (Fig 1B). To determine if Sec23
149 and Sec24 participate in protonemal growth, we used transient RNA interference
150 (RNAi) to silence the *Sec23* and *Sec24* gene families. We used a region of the

151 coding sequence from a member of each subclass (Fig1A, B, solid lines under
152 gene models). These sequence regions share a high degree of sequence similarity
153 to the other gene in each subclass (Fig 1A, B, dashed lines under gene models,
154 Table S1) and would effectively simultaneously silence both genes. We did not
155 target *Sec24E* since we were unable to detect a transcript.
156 By co-transforming the Sec23G RNAi construct together with a construct
157 containing the target sequences for *Sec23A*, *C* and *D*, we targeted the entire *Sec23*
158 gene family and discovered that silencing the seven *Sec23* genes leads to a
159 dramatic reduction in growth (Fig 1C, D). Surprisingly, we found that silencing
160 subclass III comprised of *Sec23D* and *Sec23E* resulted in a similarly severe
161 growth defect (Fig 1C and D). In contrast, silencing any of the other subclasses
162 did not affect growth (Fig 1C, D). These results demonstrated that there is
163 functional specificity among *Sec23* isoforms, with only subclass III playing a
164 critical role in protonemal growth, while the remaining five *Sec23* isoforms
165 appear to be dispensable.
166 Similar to silencing subclass III *Sec23* genes, silencing *Sec24C* and *Sec24D*
167 resulted in a 79% reduction in plant area (Fig 1E, F). Silencing *Sec24F* and
168 *Sec24G* also impaired growth, but to a lesser extent resulting in a 48% reduction
169 in plant area (Fig 1E, F). On the other hand, silencing *Sec24A* and *Sec24B* did not
170 affect growth, although both genes were expressed at high levels. These data
171 suggest that like Sec23, there is isoform specificity among *Sec24* genes.
172
173 ***Sec23 genes in subclass III are functionally redundant***
174 To test whether *Sec23D* and *Sec23E* within subclass III are functionally
175 redundant, we designed RNAi constructs targeting the untranslated regions
176 (UTRs) of each gene (Fig 2A). Targeting the untranslated regions of both *Sec23D*
177 and *Sec23E* resulted in small unpolarized plants with an 85% reduction in plant
178 area as compared to control RNAi plants (Fig 2B, C). Silencing *Sec23D* alone
179 resulted in a 59% reduction in plant area, while silencing *Sec23E* did not affect
180 plant area (Fig 2B, C). Given that *Sec23D* is expressed seven times higher than
181 *Sec23E* (Fig 1B), it is possible that *Sec23D* contributes to protonemal growth
182 more than *Sec23E*. To test whether *Sec23E* can replace *Sec23D* function if
183 expressed at sufficient levels, we performed complementation studies by driving

184 the full-length coding sequence of *Sec23D* or *Sec23E* with the constitutive maize
185 ubiquitin promoter. Interestingly, the reduction in plant area resulting from
186 silencing of *Sec23D* was restored to similar levels when either *Sec23D* or *Sec23E*
187 full-length cDNAs were expressed (Fig 2B, C), indicating that *Sec23D* and *Sec23E*
188 are functionally redundant, and that the highly expressed *Sec23D* is the
189 predominant group III isoform critical for protonemal growth.
190
191 ***CRISPR-Cas9-mediated deletion of Sec23 isoforms***
192 Using transient RNAi, we were able to deduce that *Sec23* genes display
193 isoform specific functions during protonemal growth. However transient RNAi
194 assays are limited to phenotypic characterization of 7-day-old plants. To further
195 characterize the molecular functions of *Sec23*, we generated stable loss-of-
196 function mutants of *Sec23* genes using CRISPR-Cas9 mediated genome editing.
197 We targeted each gene with one protospacer located in the first coding exon (Fig
198 S1A, S2). We obtained single and higher-order mutants of *Sec23* genes carrying
199 out-of-frame mutations resulting in premature stop codons in their transcripts
200 (Fig S1A, S2, Table S2). Consistent with the RNAi results, 7-day-old *Δsec23d*
201 plants were 70% smaller than wild type plants while *Δsec23e* plants exhibited no
202 growth defects (Fig 3A, B). We isolated a number of *sec23d* null alleles (Fig S1A,
203 Table S2), which had similar growth phenotypes (Figure S1B). We also found
204 that in three-week-old plants regenerated from protoplasts, *Δsec23d-5* plants
205 were 62.6% smaller than wild type (Fig 3C, D), and Δ*sec23d-5* had fewer
206 gametophores compared to wild type (Fig 3C, E), suggesting that slow growing
207 protonemal tissues resulted in a developmental delay in the production of
208 gametophores.
209 Although it was possible to isolate many *Δsec23d* and *Δsec23e* single
210 mutants, we were unable to obtain *Δsec23de* double mutants either by targeting
211 *Sec23D* and *Sec23E* simultaneously or by targeting *Sec23D* in the *Δsec23e-6* single
212 mutant background. This suggests that deleting both *Sec23D* and *Sec23E* is
213 incompatible with protoplast regeneration, consistent with the severe growth
214 defects observed by simultaneously silencing *Sec23D* and *Sec23E* using RNAi.
215 Furthermore, we confirmed that none of the other *Sec23* genes were upregulated

216 in *Δsec23d-5* plants (Fig S1C), suggesting that the phenotypic consequences
217 observed were due specifically to loss of *Sec23D*.
218 Since the RNAi results suggested that all other *Sec23* subclasses were not
219 required for protonemal growth, we sought to isolate a stable line lacking
220 *Sec23A*, *Sec23B*, *Sec23C*, *Sec23F*, and *Sec23G* to determine if these genes
221 contribute to other aspects of plant growth and development. We successfully
222 isolated two independent quintuple mutant alleles *Δsec23abcfg-1* and
223 *Δsec23abcfg-2,* in which *Sec23A*, *Sec23B*, *Sec23C*, *Sec23F*, and *Sec23G* contained
224 lesions resulting in null alleles for each gene (Fig S2, Table S2). Most lesions were
225 small deletions or insertions. However, *Δsec23abcfg-1* contained a three
226 thousand base pair insertion in the *Sec23G* locus, still resulting in disruption of
227 the *Sec23G* locus (Fig S2, Table S2). We characterized both quintuple mutants
228 and found that while seven-day old *Δsec23abcfg-1* plants exhibited no detectable
229 growth defects, *Δsec23abcfg-2* plants exhibited a mild growth defect (Fig 3B, C).
230 However, three-week-old *Δsec23abcfg-1* plants were larger than wild type, and
231 *Δsec23abcfg-2* plants were indistinguishable from wild type (Fig 3D, E).
232 Interestingly, both *Δsec23abcfg-1* and *Δsec23abcfg-2* developed more
233 gametophores than wild type (Fig 3E), suggesting that these five *Sec23* genes
234 may negatively regulate gametophore development.
235 Even though the two quintuple mutant isolates, exhibited statistically
236 significant differences at different times in development between each other and
237 wild type, these were minor compared to the differences between wild type and
238 all isolated *Δsec23d* null mutants. To investigate whether the observed
239 differences might result from differential upregulation of *Sec23D* or *Sec23E* in the
240 *Δsec23abcfg* mutants thereby compensating for the loss of *Sec23ABCFG*
241 functions, we measured the expression levels of *Sec23D* and *Sec23E* transcripts
242 in *Δsec23abcfg-1, Δsec23abcfg-2*, and wild type. In 8-day-old plants, we found
243 that neither *Sec23D* nor *Sec23E* transcripts were elevated compared to
244 expression in wild type (Fig 3F), indicating that minor differences observed
245 between the two quintuple mutants were not readily explained by increased
246 expression of either *Sec23D* or *E*. Taken together, the phenotypic analyses of
247 stable *sec23* null plants suggest that *Sec23A, B, C, F* and *G* do not contribute

248 substantially to establishment of juvenile moss tissues under laboratory growth
249 conditions. In contrast, *Sec23D* and *E* are essential.
250
251 ***Loss of Sec23D causes ER morphology defects and ER stress***
252 As a predicted member of the COPII complex, Sec23D likely mediates ER-
253 to-Golgi transport. However, it is unclear whether the *Δsec23d* growth defect is a
254 result of a general impairment of ER-to-Golgi transport, or the lack of specific
255 cargo sorted by Sec23D needed for protonemal growth. Studies in other
256 organisms have shown that blocking COPII function alters ER morphology
257 (Novick et al., 1980) and results in elevated levels of unfolded proteins in the ER,
258 leading to activation of the ER unfolded protein response (Belden, 2001; Chung
259 et al., 2016). To analyze Sec23D's function in ER-to-Golgi transport, we
260 investigated whether loss of Sec23D affects ER morphology and the ER unfolded
261 protein response. We used CRISPR-Cas9 mediated genome editing to knock out
262 Sec23D in a line where the ER is fluorescently labeled by targeting GFP to the ER
263 lumen (Fig S1, Table S2). When imaged with a confocal microscope, *Δsec23d-B11*
264 cells exhibited numerous ER dots (Fig 4A, red and cyan boxes), and 65% of
265 protonemal filaments contained large ER aggregates (Fig 4A, green and yellow
266 boxes). Imaging with a super resolution spinning disc confocal system allowed
267 closer inspection of the aggregates (Fig. 4B). Smaller aggregates were clearly
268 comprised of accumulated tubules, while large aggregates appeared to have
269 tubules that wrapped around each other (Fig. 4B, Movie S1).
270 If changes in ER morphology result from defective secretion at ER exit
271 sites, then proteins may be inadvertently accumulating in the ER, resulting in
272 upregulation of the unfolded protein response. To test this, we analyzed the
273 expression of an ER heat shock protein (Bip), which is a well-known ER stress
274 reporter in *Arabidopsis thaliana* (Noh et al., 2003; Srivastava et al., 2013;
275 Maruyama et al., 2014; Cho and Kanehara, 2017). *P. patens* has two *Bip* paralogs,
276 *Bip1* and *Bip2*. Since *Bip2* expression is low in protonemal tissue (Ortiz-Ramírez
277 et al., 2017), we tested whether *Bip1* is affected under conditions that induce ER
278 stress. Brefeldin A (BFA) inhibits protein secretion by disrupting ER-Golgi
279 integrity (Nebenfuhr, 2002; Niu et al., 2005). We found that after a 24-hour
280 treatment of BFA, expression of *Bip1* increased by about two-fold (Fig 4C),

281 indicating that *Bip1* is a plausible ER stress reporter in *P. patens*. Interestingly,
282 *Bip1* expression increased 5-fold in *Δsec23d* compared to in wild type (Fig 4D),
283 demonstrating that *Δsec23d* suffers from severe ER stress. In contrast,
284 *Δsec23abcfg-1*, which didn't exhibit significant growth defects, had normal levels
285 of *Bip1* expression (Fig 4D), and normal ER morphology (Fig 4A).
286
287 ***Disrupting Sec23D results in reduced ER to Golgi trafficking and secretion to***
288 ***the plasma membrane***
289 ER morphology defects and elevated ER stress in *Δsec23d* suggest that
290 transport of secretory cargos might be blocked. We reasoned that proteins
291 destined to the Golgi and the plasma membrane would accumulate in the ER in
292 mutants with impaired ER to Golgi transport. To test this, we disrupted *Sec23D*
293 in lines that either express YFP fused to the first 49 amino acids of the soybean
294 α-1,2-mannosidase, a Golgi resident protein (YFP-MAN), (Nelson et al., 2007;
295 Furt et al., 2012) or an mCherry fusion of a transmembrane protein (F-SNAP-
296 mCherry) previously used to measure exocytosis (van Gisbergen et al., 2018)
297 (Fig S1, Table S2). Since it would have been time-consuming to regenerate
298 quintuple mutants in these two backgrounds, we instead transformed the YFP-
299 MAN and F-SNAP-mCherry markers into *Δsec23abcfg-1* plants. We selected lines
300 that had similar expression levels to control lines by measuring the total amount
301 of fluorescence in cells.
302 In control YFP-MAN lines, YFP signal accumulated in the Golgi with very
303 little fluorescence observed in the rest of the cell (Fig 5A). In contrast in *Δsec23d-*
304 *F12*, while YFP fluorescence still accumulated in the Golgi, a large portion of the
305 fluorescent signal that was presumably retained in the ER was observed
306 diffusely throughout the cell (Fig 5A). To quantify ER to Golgi trafficking
307 efficiency, we calculated the fluorescence intensity ratio of the signal in the Golgi
308 divided by the signal in the cytoplasm. A high ratio value indicates efficient
309 delivery to the Golgi, as observed in the control lines (Fig 5B). In contrast,
310 *Δsec23d-F12* exhibited a significantly lower fluorescence intensity ratio (Fig 5B),
311 indicating that loss of Sec23D impairs delivery of YFP-MAN to the Golgi. Imaging
312 of *Δsec23abcfg-1* YFP-MAN and its control line revealed that the majority of the
313 YFP signal localizes to the Golgi with the Golgi to cytoplasm ratios in

314 *Δsec23abcfg*-1 indistinguishable from the control (Fig 5B), suggesting that
315 trafficking of YFP-MAN to the Golgi is not affected in the quintuple mutant.
316 Many proteins transported in COPII-coated vesicles ultimately reside at the
317 plasma membrane, are secreted, or are trafficked to the vacuole. Without a
318 fluorescent vacuolar cargo in hand, we instead investigated vacuolar
319 morphology by staining the vacuole with MDY-64, a dye that stains the tonoplast
320 in living plant cells (Scheuring et al., 2015). While we found that vacuolar
321 morphology was similar between wild type, *Δsec23d-5* and *Δsec23abcfg-1* plants
322 (Fig S3), we can not rule out that vacuolar protein sorting has not been affected.
323 To investigate trafficking to the plasma membrane, we used an engineered
324 fluorescent protein cargo, F-SNAP-mCherry, previously used to analyze
325 exocytosis in protonemata (van Gisbergen et al., 2018). In wild type cells, the F-
326 SNAP-mCherry accumulated on the plasma membrane, with only a very small
327 amount of fluorescence detected inside the cell (Fig 5C). In *Δsec23d-S2,* a large
328 portion of the mCherry signal was retained in the cell, labeling the ER network
329 (Fig 5C). To quantify secretion efficiency to the plasma membrane, we calculated
330 the fluorescence intensity ratio of the plasma membrane to the intensity within
331 the cell. We found that the ratio in *Δsec23d-S2* was significantly lower than that
332 of its control line (Fig 5D), indicating that loss of Sec23D inhibits secretion of
333 plasma membrane proteins.
334 Interestingly, we found that the F-SNAP-mCherry signal was also retained
335 inside the cell in the *Δsec23abcfg-1* mutant, readily observing labeling of the ER
336 network (Fig 5C). In addition, the fluorescence intensity ratio in *Δsec23abcfg-1*
337 was lower in comparison to the ratio in its control line (Fig 5D). However, the
338 ratio in *Δsec23abcfg-1* was still significantly higher than the ratio in *Δsec23d-S2*,
339 suggesting that secretion of plasma membrane proteins is impaired in
340 *Δsec23abcfg-1* but to a lower extent than in *Δsec23d-S2*. These data together with
341 the lack of a growth defect in protonomata in the *Δsec23abcfg-1* mutant suggest
342 that Sec23A, B, C, F, and G contribute to protein secretion particularly to the
343 plasma membrane, but importantly their cargos are not essential for polarized
344 growth in protonemata.
345

346 ***Loss of Sec23D does not affect the cytoskeleton during tip growth***

347 To investigate if defects in protein secretion, resulted in alterations to the
348 cytoskeleton, critical for polarized expansion in protonemata, we imaged
349 microtubules and actin in wild type and in cells carrying null mutations in
350 *Sec23D*. Microtubules align along the length of the cell with their plus ends
351 focused just below the cell apex (Hiwatashi et al., 2014), where a dynamic
352 cluster of actin filaments forms predicting the site of cell expansion (Wu et al.,
353 2018). Wild type and *Δsec23d-M4* cells expressing GFP-tubulin exhibit
354 indistinguishable microtubule networks and both have a focal point of
355 microtubules near the cell tip (Fig S4A, arrows). Using lifeact-mCherry to label
356 the actin network, we found that both wild type and *Δsec23d-5* cells form an
357 apical actin cluster that associates with the growing tip (Fig S4B). Time-lapse
358 imaging revealed no discernable differences in the dynamics of the apical actin
359 cluster between wild type and *Δsec23d-5* (Fig S4C, Movie S2). These data suggest
360 that tip growth defects in cells lacking Sec23D are independent of the
361 cytoskeleton.

362

363 ***Sec23 isoforms localize to discrete puncta associated with the ER***

364 If Sec23 is a bona fide COPII component, then we would expect that Sec23
365 isoforms should associate with the ER. To test this, we inserted sequences in the
366 genome of a line expressing GFP in the ER lumen encoding for three tandem
367 mRuby2 (hereafter, 3XmRuby) in frame with the coding sequences of the three
368 mostly highly expressed protonemal *Sec23* genes: *Sec23B*, *Sec23D* and *Sec23G*
369 (Fig 1B, Fig S5A, B). To ensure that tagging *Sec23D* did not affect its function, we
370 measured plant area from 7-day old regenerated protoplasts and found that
371 *Sec23D-3XmRuby* grew indistinguishably from the control lines (Fig S5C),
372 suggesting that Sec23D-mRuby is functional. By analogy, we reasoned that
373 tagging *Sec23B* and *G* would also be functional. To ensure we did not observe any
374 possible dominant negative impacts as a result of the tagging, we performed
375 growth assays of 7-day old plants regenerated from protoplasts and observed
376 that *Sec23B-3XmRuby* was indistinguishable from the control and *Sec23G-mRuby*
377 was slightly smaller (Fig S5C).

378 Imaging with confocal microscopy revealed that Sec23D, Sec23B and
379 Sec23G localized to punctate structures throughout the cytoplasm (Fig 6A). All
380 three proteins labeled puncta that were often proximal to the ER (Fig 6A). Co-
381 localization measurements using Pearson's Correlation Coefficient suggested
382 that Sec23D, B and G puncta positively correlated with the ER. To ensure that
383 this correlation was significant, we flipped the ER image both vertically and
384 horizontally and repeated the correlation analysis and found that the correlation
385 coefficients were significantly lower (Fig 6B). Interestingly, Sec23G-3XmRuby
386 puncta were larger than the punctate structures found in Sec23D- and Sec23B-
387 3XmRuby lines (Fig 6A, C). To quantify possible size differences, we imaged all
388 three tagged Sec23 isoforms with a pixel size that maximizes the resolving
389 capacity of the imaging system (Fig 6C, see Materials and Methods) and utilized a
390 segmentation tool in Fiji that identifies particles in the images (Gilles et al.,
391 2017). We discovered that Sec23G particles are significantly larger than Sec23B
392 and D. Furthermore, Sec23D is slightly larger than Sec23B. These data suggest
393 that Sec23 isoforms form distinct compartments on the ER.
394
395 ***Sec23B and Sec23G localization is independent of Sec23D.***
396 To further probe the nature of the Sec23 particles, we analyzed the
397 localization of Sec23B and Sec23G with respect to Sec23D. We used CRISPR-Cas9
398 mediated homology directed repair (HDR) to insert sequences encoding for
399 mNeonGreen (hereafter, mNeon) in-frame with Sec23B or Sec23G in a Sec23D
400 line endogenously tagged with a single mRuby2 (hereafter, mRuby) (Fig S6). As
401 expected Sec23B-mNeon formed small puncta whereas Sec23G-mNeon formed
402 larger puncta (Fig 7A, B). Imaging of Sec23B-mNeon and Sec23D-mRuby
403 revealed the presence of a distribution of cytoplasmic puncta, some with only
404 Sec23B-mNeon or only Sec23D-mRuby and some with both (Fig 7A). In contrast,
405 Sec23G-mNeon and Sec23D-mRuby were largely non-overlapping (Fig 7B). To
406 quantify the degree of overlap, we utilized the segmentation tool in Fiji that
407 identifies puncta and then determines the number of segmented particles that
408 physically overlap (Gilles et al., 2017). We found that 57% of Sec23B-mNeon co-
409 localized with Sec23-mRuby. In contrast, only 4% of Sec23G-mNeon showed
410 overlap with Sec23-mRuby (Fig 7C). In addition to identifying co-localizing

411 particles, the tool also measures the center-to-center distance of overlapping
412 particles (Gilles et al., 2017). Sec23G-mNeon and Sec23-mRuby had a
413 significantly larger center-to-center distance as compared to Sec23B-mNeon and
414 Sec23D-mRuby (Fig 7D), suggesting that any overlap between Sec23G and
415 Sec23D is coincidental.
416 While Sec23B and Sec23D exhibited a high degree of co-localization,
417 COPII vesicles are significantly smaller than the limit of resolution of a light
418 microscope. Therefore, it is unclear if a single vesicle contains both Sec23B and
419 Sec23D or if vesicles form with a single Sec23 isoform. Given that Sec23G
420 structures are distinct from Sec23D, and 40% of Sec23B and Sec23D puncta are
421 not overlapping, we hypothesized that Sec23B, Sec23D and Sec23G form distinct
422 ER exit sites. If this is the case, we would expect that Sec23B and Sec23G would
423 be unaffected by loss of Sec23D. Indeed, we discovered that when we deleted
424 Sec23D in the Sec23B-3XmRuby and Sec23G-3XmRuby lines, both Sec23B and
425 Sec23G still localized to puncta (Fig 7E). We quantified the size of the puncta and
426 found that Sec23G-3XmRuby was unaffected but Sec23B-3XmRuby were slightly
427 larger in the absence of Sec23D (Fig 7F). However, given that the average
428 Sec23B-3XmRuby particle size is essentially at the limit of resolution of our
429 system, it is unclear how significant this increase may be. Nevertheless, these
430 results demonstrate that even when ER morphology is affected due to loss of
431 Sec23D, Sec23B and Sec23G are largely unaffected, suggesting that Sec23B and
432 Sec23G ER exit sites are independent of Sec23D.
433
434 **Discussion**
435 The large number of genes encoding components of COPII in plants
436 together with functional studies in Arabidopsis (De Craene et al., 2014; Chung et
437 al., 2016; Barlow and Dacks, 2018; Brandizzi, 2018; Faso et al., 2009; Qu et al.,
438 2017; Tanaka et al., 2013) have led to the hypothesis that gene expansion
439 underlies increased functional diversification required for complex secretory
440 processes that pattern and build plant cells. Evidence suggests that functional
441 diversification could stem from tissue/developmental specific expression (Hino
442 et al., 2011; Lee et al.; Hanton et al., 2009) or from the formation of COPII
443 complexes comprised of specific isoforms with unique functions (Zeng et al.,

444 2015; Zeng et al., 2021). However, it remains unclear whether unique COPII
445 complexes mediate transport of specific cargos or accumulate at some ER exit
446 sites and not at others. Here, by analyzing the role of Sec23 and Sec24 isoforms
447 in protonemal development, we have provided evidence for formation of distinct
448 ER exit sites and the requirement of only Sec23D/E for transport of cargos
449 uniquely required for tip growth.

450 Using RNAi, we showed that *Sec23* and *Sec24* isoforms differentially
451 impact protonemal growth. Silencing of *Sec23D/E* or *Sec24C/D* similarly inhibit
452 tip growth suggesting that *Sec23D/E* may interact with *Sec24C/D*. However,
453 *Sec24F/G* also exhibited reduced growth. Thus, it is possible that a number of
454 heterodimer pairs may form that are critical for polarized growth. Protein-
455 protein interactions studies are needed to confirm if isoform specific
456 heterodimers form in moss. If this is the case, it suggests that isoform specificity
457 regulates COPII function similar to the finding in Arabidopsis that Sar1A and
458 Sec23A form a unique interaction mediating functional specificity (Zeng et al.,
459 2015).

460 Focusing on *Sec23*, where one of the Sec23 pairs, Sec23D/E, plays an
461 essential role in protonemal growth, we found several lines of evidence
462 suggesting that Sec23D functions as a bona fide COPII component. First, *Δsec23d*
463 plants had abnormal ER morphology and elevated ER stress consistent with a
464 block in cargo secretion from the ER. Second, trafficking to the Golgi and
465 secretion to the plasma membrane was reduced in *Δsec23d*. Third, Sec23D
466 localized to puncta near the ER. Due to differential expression levels, we found
467 that Sec23D is more important for protonemal growth than Sec23E. However,
468 when expressed at sufficient levels, Sec23E can rescue loss of Sec23D indicating
469 that Sec23D and Sec23E are functionally redundant. The inability to recover a
470 double mutant lacking both Sec23D and E suggests that together these two genes
471 are essential for moss viability. Given that viability in moss is measured in the
472 ability to generate protonemata, which is a tip-growing tissue, we reason that
473 Sec23D and E are essential for tip growth. While *Δsec23d* protonemal cells grow
474 significantly slower than wild type leading to smaller plants, we were unable to
475 identify any defects in either the actin or microtubules cytoskeletons, suggesting
476 that Sec23D contributes to polarized cell expansion independent of the

477 cytoskeleton. In fact, tip growth in *Δsec23d* resembles the recently identified *P.*
478 *patens Δsabre* mutant plants (Cheng & Bezanilla, 2021). SABRE associates with
479 regions of the ER and its absence has no effect on the cytoskeleton but rather
480 impacts ER morphology by accumulating aggregates that label with an ER
481 lumenal marker (Cheng & Bezanilla, 2021). Taken together these data suggest
482 that abrogated ER function impacts polarized growth without altering
483 cytoskeletal organization and dynamics.
484 With respect to gametophore formation, *Δsec23d* develops gametophores
485 late, but once gametophores form they are morphologically normal. This
486 suggests that Sec23D function is specifically required during tip growth. In
487 contrast, we found that the remaining five *Sec23* genes were dispensable for
488 formation of both protonemata and gametophores. One possible explanation for
489 this finding is that Sec23A, B, C, F and G have functionally diversified no longer
490 playing a role in ER to Golgi transport. In support of this hypothesis, unlike
491 *Δsec23d*, *Δsec23abcfg* plants did not exhibit ER morphology defects or increased
492 ER stress characteristic of cargo backing up in the ER often observed with COPII
493 loss of function mutants. However, we did observe secretion defects of plasma
494 membrane cargo in *Δsec23abcfg* plants. Given that Sec23B and G localize
495 proximal to the ER independent of Sec23D, it is possible that Sec23B and G
496 contribute to COPII function via pathways that may potentially bypass the Golgi
497 (Cheng et al., 2009; Zhang et al., 2011; Ding et al., 2012; Wang et al., 2017).
498 Alternatively, Sec23B and G may also function in ER to Golgi trafficking but, in
499 contrast to Sec23D, their cargos may be fewer and may not be essential for tip
500 growth.
501 Interestingly all the mutant combinations that we generated formed
502 morphologically normal gametophores. However, since we were unable to
503 generate *Δsec23de* or *Δsec23abcefg* plants, we can not distinguish between
504 Sec23E playing a critical role in gametophore formation versus Sec23D or
505 Sec23E acting redundantly with Sec23A, B, C, F and G for COPII secretion
506 required to shape gametophores. If, on the other hand, COPII is not required for
507 gametophore formation, then future experiments conditionally removing
508 Sec23D/E in *Δsec23abcfg* plants would be expected to form normal
509 gametophores and would be an excellent tool to identify COPII-independent

510 secretion pathways in plants, which are thought to play a role in transport of
511 tonoplast resident proteins such as the vacuolar H^+-ATPase, VHA-a3 (Viotti et al.,
512 2013).

513 While Sec23B, Sec23D, and Sec23G formed puncta associated with the ER,
514 these puncta were distinct. Sec23G formed large dots near the ER, whereas
515 Sec23D and Sec23B were smaller. Sec23B and Sec23D puncta exhibited a high
516 degree of overlap, suggesting that Sec23B and Sec23D may form vesicles in the
517 same region of the ER. In contrast Sec23G largely did not overlap with Sec23D
518 and by extension likely not Sec23B. Formation of larger domains on the ER
519 suggests that Sec23G may be involved in the secretion of bigger cargo and
520 provides evidence that moss has morphologically distinct ER exit sites, that can
521 form, even when ER morphology is disrupted, independent of Sec23D.

522 Given that Sec23D contributes to ER to Golgi trafficking and secretion to
523 the plasma membrane, while Sec23A, B, C, F and G contributes to plasma
524 membrane secretion, it is plausible to suggest that tip growth requires intact ER
525 to Golgi trafficking. In *Δsec23d* plants cargos essential for tip growth are either
526 inefficiently carried from the ER to the Golgi or are not properly processed in the
527 Golgi due to severe reductions in trafficking to the Golgi. Perhaps there is a larger
528 burden for carbohydrates synthesized by enzymes in the Golgi to generate a tip
529 growing cell wall as compared to a diffusely growing cell wall. To test this, future
530 studies will focus on identifying cargos that have been differentially affected in
531 *Δsec23d* versus *Δsec23abcfg* plants. Comparative mass spectrometry of isolated
532 microsomes and plasma membrane extracts in these mutant backgrounds could
533 be very informative. In addition, quantitatively measuring secretion of known
534 Golgi resident carbohydrate biosynthetic enzymes and plasma membrane
535 complexes such as cellulose and callose synthases in these mutants could help to
536 narrow down cargo specificity.

537 Taking advantage of the facile molecular genetic manipulation and
538 imaging in moss protonemal development, our study has shown that the
539 expanded *Sec23* gene family in moss is multi-faceted. We found evidence that the
540 *Sec23* gene family exhibits aspects of functional redundancy, differential gene
541 expression, as well as isoform specificity for ER exit site formation, ER to Golgi
542 trafficking, and importantly transport of essential cargos required for tip growth.

543 Building upon the tools developed in this study, future studies will be able to
544 characterize the remaining COPII components, thereby providing a complete
545 picture of how gene expansions in COPII have been deployed.

546 **Materials and Methods**

547 ***Expression analyses***

548 To quantify expression of the *Sec23* and *Sec24* genes family members
549 (Table S3), as well as *Bip1* (Pp3c10_17310), we isolated total RNA from 8-day old
550 plants (various genotypes, as needed for the particular experiment) regenerated
551 from protoplasts using the RNeasy Plant mini prep kit (Qiagen). cDNA was
552 prepared from 1µg of total RNA using SuperScriptIII reverse transcriptase kit,
553 following the manufacturer's recommendation (Invitrogen). qPCR assays were
554 conducted with Luna Universal qPCR Master Mix (New England Biolabs).
555 Primers for qRT-PCR analyses are listed in Table S4. After confirming that
556 amplification efficiencies (calculated from standard curves) were similar for
557 each set of primers (Table S4), relative expression levels were calculated, and
558 expression of Ubiquitin 10 was used for normalization. All experiments had
559 three technical replicates and three biological replicates.

560

561 ***Constructs***

562 The Sec23 and Sec24 RNAi constructs were generated by PCR
563 amplification of either the coding sequence or 5' and 3' untranslated region
564 (UTR) of *Sec23* or *Sec24* from *P. patens* cDNA using primers indicated in Table S4.
565 PCR fragments were cloned into pENTR-D-TOPO (Invitrogen) following the
566 manufacturer's recommendations and the resulting vectors were sequenced. The
567 Sec23ACD-RNAi and Sec23 UTR-RNAi constructs were generated by stitching
568 together multiple PCR fragments and then directionally cloned into pENTR-D-
569 TOPO as previously described (Vidali et al., 2007). LR clonase (Invitrogen)
570 reactions were used to transfer either the coding sequence or 5' and 3' UTR
571 sequences the RNAi vector pUGGi (Bezanilla et al., 2005) generating the Sec23
572 UTRi or Sec24-CDSi constructs, respectively. Restriction enzyme digestion was
573 used to verify these constructs.

574 Expression constructs were generated by PCR amplifying *Sec23D* and
575 *Sec23E* coding sequences from *P. patens* cDNA using a 5' CACC sequence on the
576 specific primers for oriented cloning into the pENTR-D-TOPO vector
577 (Invitrogen). LR clonase (Invitrogen) reactions were used to transfer these
578 coding sequence into pTH-Ubi-Gate vectors (Vidali et al., 2007).

579 *Sec23* tagging constructs were generated by PCR amplifying genomic
580 sequences upstream and downstream of the stop codon for *Sec23D*, *Sec23B*, and
581 *Sec23G* using the primers in Table S4. For *Sec23D*, we used homologous
582 recombination. The distance between the 5' and 3' homology arms was 500bp,
583 which when inserted correctly the tagging construct replaces these 500bp with
584 sequences encoding for the fluorescent protein and an antibiotic resistance
585 cassette (Fig S5, Fig S6). Using BP clonase (Invitrogen), homology arms were
586 transferred to vectors, generating homology arm entry clones. Four-fragment
587 recombination reactions were used to assemble the homology arms, fluorescent
588 protein sequence, and the antibiotic resistance cassette into pGEM-gate (Vidali et
589 al., 2009). For *Sec23B* and *Sec23G* tagging, we used CRISPR Cas9-mediated HDR.
590 5' and 3' homology arms upstream and downstream of the stop codon, with a
591 distance between these two arms of 38bp for *Sec23B* and 131bp for *Sec23G* were
592 PCR amplified from genomic DNA (Fig S5, Fig S6). Using BP clonase (Invitrogen),
593 homology arms were transferred to vectors, generating homology arm entry
594 clones, as described in (Mallett et al., 2019). Three-fragment recombination
595 reactions were used to assemble the homology arms and the fluorescent protein
596 sequence into pGEM-gate. We chose the CRISPR-Cas9 protospacer close to the
597 stop codon.
598 Protospacers for CRISPR-Cas9 mediated mutagenesis and HDR were
599 designed with the CRISPOR online software (crispor.tefor.net) (Haeussler et al.,
600 2016). Protospacers were selected with high specificity scores and low off-target
601 frequency. Specific overhangs sequences were added to facilitate downstream
602 cloning. Protospacers were synthesized as oligonucleotides (Table S4) and
603 annealed as described (Mallett et al., 2019). Annealed protospacer fragments
604 were transferred to vectors using Instant Sticky-End Ligation Master Mix (New
605 England Biolabs). *Sec23B* and *G* protospacers designed to tag these genes via
606 HDR as well as *Sec23A*, *D* and *E* protospacers designed to knock out these genes
607 were ligated into pENTR-PpU6-sgRNA-L1L2 (Mallett et al., 2019). *Sec23B* and *F*
608 protospacers designed to knock out these genes were ligated into pENTR-PpU6-
609 sgRNA-L1L5 (Mallett et al., 2019). Sec23C and G protospacers designed to knock
610 out these genes were ligated into pENTR-PpU6-sgRNA-R5L2 (Mallett et al.,
611 2019). LR clonase (Invitrogen) was used to assemble the protospacer containing

612 vectors into pZeo-Cas9-Gate, pMH-Cas9-Gate, or pMK-Cas9-Gate vectors (Mallett
613 et al., 2019), as needed. Two-fragment recombination reactions were used to
614 assemble dual targeting mutagenesis vectors for *Sec23B* and *C*, and for *Sec23F*
615 and *G*. Restriction enzyme digestion and sequencing was used to verify these
616 constructs.
617
618 ***Tissue propagation, transformation, and genotyping***
619 All moss lines were propagated weekly by moderate homogenization in
620 water and pipetting onto a permeable cellophane covered solid media, as
621 described previously (Wu and Bezanilla, 2014). Tissue was grown at room
622 temperature in Percival growth chambers, under 85 $\mu mol_{photons}/m^2s$ light with
623 long-day conditions. PEG-mediated transformations were performed as
624 previously described to generate stable lines (Wu and Bezanilla, 2014), CRISPR-
625 Cas9 genome edited lines (Mallett et al., 2019) and perform transient RNAi
626 (Vidali et al., 2007).
627 To genotype mutants generated by CRISPR-Cas9 mutagenesis, we
628 extracted DNA from plants that were 3-4 weeks old (0.5-1cm in diameter) using
629 the protocol described in (Augustine et al., 2011). For editing experiments, we
630 used primers (Table S4) surrounding the expected Cas9 cleavage site (~300-400
631 bp on each side). T7 endonuclease assay was used to screen candidate mutants
632 as described (Mallett et al., 2019). For homology-directed repair tagging and
633 homologous recombination tagging, we used primers (Table S4) outside of the
634 homology region to avoid amplification of residual DNA donor template.
635
636 ***Imaging and morphometric analysis of growth assays***
637 For transient RNAi, complementation analyses, and growth assays of
638 stable lines, plants regenerated from protoplasts were photographed seven days
639 after protoplasting. For transient RNAi and complementation analyses plants
640 lacking nuclear GFP signal were imaged because these are the plants that are
641 actively silencing as described previously (Bezanilla et al., 2005; Vidali et al.,
642 2007). For growth assays of stable lines any regenerated plant was imaged.
643 Images were acquired with a 1X objective using a stereomicroscope (Leica
644 MZ16FA or Nikon SMZ25) equipped with a CCD camera (Leica DF300FX or

645 Nikon digital sight DS-Fi2). Chlorophyll fluorescence and any nuclear GFP signal
646 were acquired simultaneously using filters (480/40, dichroic 505 (Leica) or
647 dichroic 510 (Nikon), emission 510 long pass). Exposure settings were
648 maintained constant throughout an experiment. 3-week old plants regenerated
649 from protoplasts were imaged with white light on a Nikon SMZ25
650 stereomicroscope equipped with a Nikon digital sight DS-Fi2 color camera.
651 To quantify plant area, individual plants were cropped from images and
652 the red channel, representing chlorophyll fluorescence of the plant, was
653 separated from the RGB image. Threshold settings were set manually for all
654 plants within an experiment. To quantify brightfield images of 3-week-old plants,
655 the blue channel, representing chlorophyll fluorescence of the plant, was
656 separated from the RGB image and thresholded. Total area was calculated from
657 the largest thresholded object in the selected window. All images analysis was
658 done using macros (Galotto et al., 2019) written for ImageJ. Analysis of variation
659 (ANOVA) for multiple comparisons was performed with Kaleidagraph (Synergy)
660 using the Tukey HSD post hoc tests. The alpha for statistical significance was set
661 to 0.05.
662
663 ***Laser scanning confocal microscope imaging and quantification***
664 For imaging Sec23B/D/G localization and dynamics, 5 to 8-day old plants
665 regenerated from protoplasts were placed onto an agar pad in Hoagland's buffer
666 (4mM KNO_3, 2mM KH_2PO_4, 1mM $Ca(NO_3)_2$, 89µM Fe citrate, 300µM $MgSO_4$,
667 9.93µM H_3BO_3, 220nM $CuSO_4$, 1.966µM $MnCl_2$, 231nM $CoCl_2$, 191nM ZnSO4,
668 169nM KI, 103nM Na_2MoO_4, and 1% sucrose), covered by a glass cover slip and
669 sealed with VALAP (1:1:1 parts of Vaseline, lanoline, and paraffin). For imaging
670 ER morphology, Golgi resident protein secretion, F-SNAP-mCherry secretion, we
671 used microfluidic imaging chambers (Bascom et al., 2016). Ground protonemal
672 tissue was gently pipetted into the central part of the device followed by an
673 infusion of Hoagland's medium. Then the chamber was submerged Hoagland's
674 medium, and placed under constant 85 $\mu mol_{photons}/m^2s$ light.
675 Images were acquired on a Nikon A1R confocal microscope system with a
676 1.49 NA 60X oil immersion objective (Nikon) at room temperature. Image
677 acquisition was controlled by NIS-Element AR 4.1 software (Nikon). Laser

678 illumination at 488 nm was used for exciting mNeon, YFP, GFP and chlorophyll
679 autofluorescence; 561 nm for mRuby, mCherry. Emission filters were 525/50
680 nm for mNeon, YFP, and GFP; 595/50 nm for mRuby and mCherry.
681 Super resolution spinning disc confocal imaging was performed with a
682 Nikon CSUW1-SoRA system. Images were acquired with a 60x Plan Apo 1.40NA
683 objective with the 2.8x mag lens. Laser illumination at 488 nm was used for
684 exciting GFP, and the Emission filter were 525/50. Images were denoised using
685 the denoise.ai machine learning algorithm and deconvolved using the
686 Richardson-Lucy algorithm within the NIS-Elements v5.21 software.
687 For quantification of trafficking to the Golgi, confocal Z-stacks of
688 individual cells were converted to a maximum intensity projection. For
689 quantification of secretion to the plasma membrane, the medial focal plane was
690 selected for analysis. YFP (YFP-MAN) and mCherry (FSnap-mCherry)
691 fluorescence intensities with the same expression pattern were normalized
692 using enhanced contrast in Fiji. Images were cropped to isolate regions only
693 within the cell. Then, using a minimum threshold of 20,000-22,000 it was
694 possible to isolate and measure the fluorescence intensity of the Golgi structures
695 (Golgi intensity) or the plasma membrane with analyze particles in Fiji. The
696 fluorescence intensity of the background was similarly measured using the same
697 threshold cut-off for each image but unchecking dark background, thereby
698 selecting all regions below the threshold cut off. These values were used to
699 calculate the ratio of Golgi/plasma membrane intensity to background intensity.
700 To quantify the Pearson's Correlation Coefficient, we analyzed single focal planes
701 with the Coloc2 plugin in Fiji comparing the original images as well as
702 horizontally and vertically flipped ER-GFP images. To quantify the size and co-
703 localization of Sec23B, D and G dots, we analyzed single focal planes and used the
704 diAna tool for ImageJ, which uses object-based identification for distance and co-
705 localization measurements (Gilles et al., 2017) and was recently used to define
706 specific subdomains of the trans Golgi network in plant cells (Heinze et al.,
707 2020). All images were acquired with a pixel size of 0.07 μm and processed by
708 subtracting background, enhancing contrast with normalization, and smoothing
709 in Fiji prior to performing segmentation with diAna. For Sec23G-mNeon,
710 chloroplast autofluorescence was collected in the far-red channel and subtracted

711 from the green channel. To segment the dots in the image, we used the iterative
712 option with a minimum threshold of 25,000-27,500 and a step value of 20. After
713 segmentation, the diAna analyse module was used to measure the size of all
714 segmented regions of an image, as well as to determine the percent of co-
715 localizing particles. For particles that did overlap, we also extracted the center-
716 to-center distance of those overlapping particles. For all data, analysis of
717 variation (ANOVA) for multiple comparisons was performed with Kaleidagraph
718 (Synergy) using the Tukey HSD post hoc tests. The alpha for statistical
719 significance was set to 0.05. For pairwise comparisons, a student-T test was used
720 using Kaleidagraph (Synergy).
721
722
723 **Author contributions**
724 M.C. and M.B. designed the research. M.C., S.W., J.E.O. and S.E.R performed
725 the research. M.C., S.W. and M.B. wrote the manuscript.
726
727 **Acknowledgements**
728 We thank members of the Bezanilla lab for careful reading of the
729 manuscript. M.C. received support from the Plant Biology Graduate Program at
730 the University of Massachusetts, Amherst. This work was supported by
731 Dartmouth College and grants from the National Science Foundation (MCB-
732 1330171 and MCB-1715785 to M.B.).
733
734 **References**
735 Aridor, M. (2018). COPII gets in shape: Lessons derived from morphological
736 aspects of early secretion. Traffic 19: 823–839.
737
738 Aridor, M., Fish, K.N., Bannykh, S., Weissman, J., Roberts, T.H., Lippincott-
739 Schwartz, J., and Balch, W.E. (2001). The Sar1 Gtpase Coordinates
740 Biosynthetic Cargo Selection with Endoplasmic Reticulum Export Site
741 Assembly. Journal of Cell Biology 152: 213–230.
742
743 Aridor, M., Weissman, J., Bannykh, S., Nuoffer, C., and Balch, W.E. (1998). Cargo
744 Selection by the COPII Budding Machinery during Export from the ER.
745 Journal of Cell Biology 141: 61–70.

746 Augustine, R.C., Pattavina, K.A., Tüzel, E., Vidali, L., and Bezanilla, M. (2011). Actin
747 interacting protein1 and actin depolymerizing factor drive rapid actin
748 dynamics in Physcomitrella patens. Plant Cell 23: 3696–3710.
749
750 Barlow, L.D. and Dacks, J.B. (2018). Seeing the endomembrane system for the
751 trees: Evolutionary analysis highlights the importance of plants as models
752 for eukaryotic membrane-trafficking. Seminars in Cell & Developmental
753 Biology 80: 142–152.
754
755 Barlowe, C. (2003). Signals for COPII-dependent export from the ER: what's the
756 ticket out? Trends in Cell Biology 13: 295–300.
757
758 Barlowe, C. and Helenius, A. (2016). Cargo Capture and Bulk Flow in the Early
759 Secretory Pathway. Annu. Rev. Cell Dev. Biol. 32: 197–222.
760
761 Barlowe, C. and Schekman, R. (1993). SEC12 encodes a guanine-nucleotide-
762 exchange factor essential for transport vesicle budding from the ER.
763 Nature 365: 347–349.
764
765 Bascom, C.S., Wu, S.-Z., Nelson, K., Oakey, J., and Bezanilla, M. (2016). Long-Term
766 Growth of Moss in Microfluidic Devices Enables Subcellular Studies in
767 Development. Plant Physiology 172: 28–37.
768
769 Belden, W.J. (2001). Role of Erv29p in Collecting Soluble Secretory Proteins into
770 ER-Derived Transport Vesicles. Science 294: 1528–1531.
771
772 Bezanilla, M., Perroud, P.-F., Pan, A., Klueh, P., and Quatrano, R.S. (2005). An RNAi
773 system in Physcomitrella patens with an internal marker for silencing
774 allows for rapid identification of loss of function phenotypes. Plant Biol
775 (Stuttg) 7: 251–257.
776
777 Bi, X., Corpina, R.A., and Goldberg, J. (2002). Structure of the Sec23/24–Sar1 pre-
778 budding complex of the COPII vesicle coat. Nature 419: 271–277.
779
780 Brandizzi, F. (2018). Transport from the endoplasmic reticulum to the Golgi in
781 plants: Where are we now? Seminars in Cell & Developmental Biology 80:
782 94–105.
783
784 Brandizzi, F. and Barlowe, C. (2013). Organization of the ER–Golgi interface for
785 membrane traffic control. Nat Rev Mol Cell Biol 14: 382–392.
786
787 Cheng, F-y., Zamski, E., Guo W-w., Mason Pharr, D., and Williamson, J.D. (2009).
788 Salicylic acid stimulates secretion of the normally symplastic enzyme
789 mannitol dehydrogenase: a possible defense against mannitol-secreting
790 fungal pathogens. Planta 230: 1093–1103.
791
792 Cheng, X., and Bezanilla M. (2021). SABRE populates ER domains essential for
793 cell plate maturation and cell expansion influencing cell and tissue
794 patterning. eLife 10: e65166.

795
796 Cho, Y. and Kanehara, K. (2017). Endoplasmic Reticulum Stress Response in
797 Arabidopsis Roots. Front. Plant Sci. 8.
798
799 Chung, K.P., Zeng, Y., and Jiang, L. (2016). COPII Paralogs in Plants: Functional
800 Redundancy or Diversity? Trends in Plant Science 21: 758–769.
801
802 De Craene, J.-O., Courte, F., Rinaldi, B., Fitterer, C., Herranz, M.C., Schmitt-
803 Keichinger, C., Ritzenthaler, C., and Friant, S. (2014). Study of the Plant
804 COPII Vesicle Coat Subunits by Functional Complementation of Yeast
805 Saccharomyces cerevisiae Mutants. PLoS ONE 9: e90072.
806
807 Ding, Y., Wang, J., Wang, J., Stierhof, Y-D., Robinson, D.G., and Jiang L. (2012).
808 Unconventional protein secretion. Trends in Plant Science 17: 606-615.
809
810 Faso, C., Chen, Y.-N., Tamura, K., Held, M., Zemelis, S., Marti, L., Saravanan, R.,
811 Hummel, E., Kung, L., Miller, E., Hawes, C., and Brandizzi, F. (2009). A
812 Missense Mutation in the Arabidopsis COPII Coat Protein Sec24A Induces
813 the Formation of Clusters of the Endoplasmic Reticulum and Golgi
814 Apparatus. The Plant Cell 21: 3655–3671.
815
816 Fath, S., Mancias, J.D., Bi, X., and Goldberg, J. (2007). Structure and Organization
817 of Coat Proteins in the COPII Cage. Cell 129: 1325–1336.
818
819 Furt, F., Lemoi, K., Tüzel, E., and Vidali, L. (2012). Quantitative analysis of
820 organelle distribution and dynamics in Physcomitrella patens protonemal
821 cells. BMC Plant Biol. 12: 70.
822
823 Galotto, G., Bibeau, J.P., and Vidali, L. (2019). Automated Image Acquisition and
824 Morphological Analysis of Cell Growth Mutants in Physcomitrella patens.
825 In Plant Cell Morphogenesis, F. Cvrčková and V. Žárský, eds, Methods in
826 Molecular Biology. (Springer New York: New York, NY), pp. 307–322.
827
828 Gilles, J.-F., Dos Santos, M., Boudier, T., Bolte, S., and Heck, N. (2017). DiAna, an
829 ImageJ tool for object-based 3D co-localization and distance analysis.
830 Methods 115: 55–64.
831
832 Giraudo, C.G. and Maccioni, H.J.F. (2003). Endoplasmic Reticulum Export of
833 Glycosyltransferases Depends on Interaction of a Cytoplasmic Dibasic
834 Motif with Sar1. MBoC 14: 3753–3766.
835
836 van Gisbergen, P.A.C., Wu, S.-Z., Chang, M., Pattavina, K.A., Bartlett, M.E., and
837 Bezanilla, M. (2018). An ancient Sec10-formin fusion provides insights
838 into actin-mediated regulation of exocytosis. J. Cell Biol. 217: 945–957.
839
840 Haeussler, M., Schönig, K., Eckert, H., Eschstruth, A., Mianné, J., Renaud, J.-B.,
841 Schneider-Maunoury, S., Shkumatava, A., Teboul, L., Kent, J., Joly, J.-S., and
842 Concordet, J.-P. (2016). Evaluation of off-target and on-target scoring

843 algorithms and integration into the guide RNA selection tool CRISPOR.
844 Genome Biol. 17: 148.
845
846 Hanna, M.G., Peotter, J.L., Frankel, E.B., and Audhya, A. (2018). Membrane
847 Transport at an Organelle Interface in the Early Secretory Pathway: Take
848 Your Coat Off and Stay a While: Evolution of the metazoan early secretory
849 pathway. BioEssays 40: 1800004.
850
851 Hanton, S.L., Matheson, L.A., Chatre, L., and Brandizzi, F. (2009). Dynamic
852 organization of COPII coat proteins at endoplasmic reticulum export sites
853 in plant cells. The Plant Journal 57: 963–974.
854
855 Heinze, L., Freimuth, N., Rößling, A.-K., Hahnke, R., Riebschläger, S., Fröhlich, A.,
856 Sampathkumar, A., McFarlane, H.E., and Sauer, M. (2020). EPSIN1 and
857 MTV1 define functionally overlapping but molecularly distinct trans-Golgi
858 network subdomains in Arabidopsis. PNAS 117: 25880–25889.
859
860 Hino, T., Tanaka, Y., Kawamukai, M., Nishimura, K., Mano, S., and Nakagawa, T.
861 (2011). Two Sec13p Homologs, AtSec13A and AtSec13B, Redundantly
862 Contribute to the Formation of COPII Transport Vesicles in *Arabidopsis*
863 *thaliana*. Bioscience, Biotechnology, and Biochemistry 75: 1848–1852.
864
865 Hiwatashi, Y., Sato, Y., and Doonan, J.H. (2014). Kinesins Have a Dual Function in
866 Organizing Microtubules during Both Tip Growth and Cytokinesis in
867 Physcomitrella patens. The Plant Cell 26: 1256–1266.
868
869 Jensen, D. and Schekman, R. (2011). COPII-mediated vesicle formation at a
870 glance. Journal of Cell Science 124: 1–4.
871
872 Khoriaty, R. et al. (2018). Functions of the COPII gene paralogs SEC23A and
873 SEC23B are interchangeable in vivo. Proc Natl Acad Sci USA 115: E7748–
874 E7757.
875
876 Lee, M.H., Lee, S.H., Kim, H., Jin, J.B., Kim, D.H., and Hwang, I. A WD40 Repeat
877 Protein, Arabidopsis Sec13 Homolog 1, May Play a Role in Vacuolar
878 Trafficking by Controlling the Membrane Association of AtDRP2A.: 10.
879
880 Mallett, D.R., Chang, M., Cheng, X., and Bezanilla, M. (2019). Efficient and modular
881 CRISPR-Cas9 vector system for Physcomitrella patens. Plant Direct 3:
882 e00168-15.
883
884 Mancias, J.D. and Goldberg, J. (2007). The Transport Signal on Sec22 for
885 Packaging into COPII-Coated Vesicles Is a Conformational Epitope.
886 Molecular Cell 26: 403–414.
887
888 Maruyama, D., Sugiyama, T., Endo, T., and Nishikawa, S. (2014). Multiple BiP
889 Genes of Arabidopsis thaliana are Required for Male Gametogenesis and
890 Pollen Competitiveness. Plant and Cell Physiology 55: 801–810.
891

892 Mossessova, E., Bickford, L.C., and Goldberg, J. (2003). SNARE selectivity of the
893 COPII coat. Cell 114: 483–495.
894
895 Nakano, A. and Muramatsu, M. (1989). A Novel GTP-binding Protein, Sarlp, Is
896 Involved in Transport from the Endoplasmic Reticulum to the Golgi
897 Apparatus. The Journal of Cell Biology 109: 2677–2691.
898
899 Nakano, R.T., Matsushima, R., Ueda, H., Tamura, K., Shimada, T., Li, L., Hayashi, Y.,
900 Kondo, M., Nishimura, M., and Hara-Nishimura, I. (2009). GNOM-
901 LIKE1/ERMO1 and SEC24a/ERMO2 Are Required for Maintenance of
902 Endoplasmic Reticulum Morphology in Arabidopsis thaliana. The Plant
903 Cell 21: 3672–3685.
904
905 Nebenfuhr, A. (2002). Brefeldin A: Deciphering an Enigmatic Inhibitor of
906 Secretion. Plant physiology 130: 1102–1108.
907
908 Nelson, B.K., Cai, X., and Nebenführ, A. (2007). A multicolored set of in vivo
909 organelle markers for co-localization studies in Arabidopsis and other
910 plants. Plant J. 51: 1126–1136.
911
912 Niu, T.-K., Pfeifer, A.C., Lippincott-Schwartz, J., and Jackson, C.L. (2005). Dynamics
913 of GBF1, a Brefeldin A-Sensitive Arf1 Exchange Factor at the Golgi□V.
914 Molecular Biology of the Cell 16: 1213–1222.
915
916 Noh, S.-J., Kwon, C.S., Oh, D.-H., Moon, J.S., and Chung, W.-I. (2003). Expression of
917 an evolutionarily distinct novel BiP gene during the unfolded protein
918 response in Arabidopsis thaliana. Gene 311: 81–91.
919
920 Novick, P., Field, C., and Schekman, R. (1980). Identification of 23
921 complementation groups required for post-translational events in the
922 yeast secretory pathway. Cell 21: 205–215.
923
924 Nufer, O. (2003). ER export of ERGIC-53 is controlled by cooperation of targeting
925 determinants in all three of its domains. Journal of Cell Science 116:
926 4429–4440.
927
928 Ortiz-Ramírez, C., Michard, E., Simon, A.A., Damineli, D.S.C., Hernandez-Coronado,
929 M., Becker, J.D., and Feijó, J.A. (2017). GLUTAMATE RECEPTOR-LIKE
930 channels are essential for chemotaxis and reproduction in mosses. Nature
931 549: 91–95.
932
933 Qu, X., Zhang, R., Zhang, M., Diao, M., Xue, Y., and Huang, S. (2017). Organizational
934 innovation of apical actin filaments drives rapid pollen tube growth and
935 turning. Mol Plant 10: 930–947.
936
937 Rensing, S.A., Goffinet, B., Meyberg, R., Wu, S.-Z., and Bezanilla, M. (2020). The
938 Moss *Physcomitrium* (*Physcomitrella*) *patens* : A Model Organism for
939 Non-Seed Plants. Plant Cell 32: 1361–1376.
940

941 Robinson, D.G., Brandizzi, F., Hawes, C., and Nakano, A. (2015). Vesicles versus
942 Tubes: Is Endoplasmic Reticulum-Golgi Transport in Plants
943 Fundamentally Different from Other Eukaryotes? Plant Physiology 168:
944 393–406.
945
946 Salama, N.R., Yeung, T., and Schekman, R.W. The Secl3p complex and
947 reconstitution of vesicle budding from the ER with purified cytosolic
948 proteins. The EMBO Journal 12: 4073–4082.
949
950 Scheuring, D., Schöller, M., Kleine-Vehn, J., and Löfke, C. (2015). Vacuolar staining
951 methods in plant cells. Methods Mol Biol 1242: 83–92.
952
953 Schlacht, A. and Dacks, J.B. (2015). Unexpected Ancient Paralogs and an
954 Evolutionary Model for the COPII Coat Complex. Genome Biology and
955 Evolution 7: 1098–1109.
956
957 Srivastava, R., Deng, Y., Shah, S., Rao, A.G., and Howell, S.H. (2013). BINDING
958 PROTEIN Is a Master Regulator of the Endoplasmic Reticulum Stress
959 Sensor/Transducer bZIP28 in *Arabidopsis*. Plant Cell 25: 1416–1429.
960
961 Stagg, S.M., Gürkan, C., Fowler, D.M., LaPointe, P., Foss, T.R., Potter, C.S.,
962 Carragher, B., and Balch, W.E. (2006). Structure of the Sec13/31 COPII
963 coat cage. Nature 439: 234–238.
964
965 Stagg, S.M., LaPointe, P., Razvi, A., Gürkan, C., Potter, C.S., Carragher, B., and Balch,
966 W.E. (2008). Structural Basis for Cargo Regulation of COPII Coat
967 Assembly. Cell 134: 474–484.
968
969 Takagi, J., Renna, L., Takahashi, H., Koumoto, Y., Tamura, K., Stefano, G., Fukao, Y.,
970 Kondo, M., Nishimura, M., Shimada, T., Brandizzi, F., and Hara-Nishimura,
971 I. (2013). MAIGO5 Functions in Protein Export from Golgi-Associated
972 Endoplasmic Reticulum Exit Sites in Arabidopsis. The Plant Cell 25: 4658–
973 4675.
974
975 Tanaka, Y., Nishimura, K., Kawamukai, M., Oshima, A., and Nakagawa, T. (2013).
976 Redundant function of two Arabidopsis COPII components, AtSec24B and
977 AtSec24C, is essential for male and female gametogenesis. Planta 238:
978 561–575.
979
980 Vidali, L., Augustine, R.C., Kleinman, K.P., and Bezanilla, M. (2007). Profilin is
981 essential for tip growth in the moss Physcomitrella patens. Plant Cell 19:
982 3705–3722.
983
984 Vidali, L., van Gisbergen, P.A.C., Guérin, C., Franco, P., Li, M., Burkart, G.M.,
985 Augustine, R.C., Blanchoin, L., and Bezanilla, M. (2009). Rapid formin-
986 mediated actin-filament elongation is essential for polarized plant cell
987 growth. Proc. Natl. Acad. Sci. U.S.A. 106: 13341–13346.
988

989 Viotti, C. et al. (2013). The Endoplasmic Reticulum Is the Main Membrane Source
990 for Biogenesis of the Lytic Vacuole in *Arabidopsis*. Plant Cell 25: 3434–
991 3449.
992
993 Wang, X., Chung, K. P., Lin, W., and Jiang L. (2017). Protein secretion in plants:
994 conventional and unconventional pathways and new techniques. Journal
995 of Experimental Botany 69: 21-37.
996
997 Whittle, J.R.R. and Schwartz, T.U. (2010). Structure of the Sec13–Sec16 edge
998 element, a template for assembly of the COPII vesicle coat. The Journal of
999 Cell Biology 190: 347–361.
1000
1001 Wu, S.-Z. and Bezanilla, M. (2014). Myosin VIII associates with microtubule ends
1002 and together with actin plays a role in guiding plant cell division. eLife
1003 Sciences 3: e03498.
1004
1005 Wu, S.-Z., Yamada, M., Mallett, D.R., and Bezanilla, M. (2018). Cytoskeletal
1006 discoveries in the plant lineage using the moss Physcomitrella patens.
1007 Biophys Rev 10: 1683–1693.
1008
1009 Zeng, Y., Chung, K.P., Li, B., Lai, C.M., Lam, S.K., Wang, X., Cui, Y., Gao, C., Luo, M.,
1010 Wong, K.-B., Schekman, R., and Jiang, L. (2015). Unique COPII component
1011 AtSar1a/AtSec23a pair is required for the distinct function of protein ER
1012 export in *Arabidopsis thaliana*. Proc Natl Acad Sci USA 112: 14360–14365.
1013
1014 Zeng, Y., Li, B., Ji, C., Feng, L., Niu, F., Deng, C., Chen, S., Lin, Y., Cheung, K.C.P., Shen,
1015 J., Wong, K.-B., and Jiang, L. (2021). A unique AtSar1D-AtRabD2a nexus
1016 modulates autophagosome biogenesis in Arabidopsis thaliana. Proc Natl
1017 Acad Sci U S A 118.
1018
1019 Zhang, H., Zhang, L., Gao, B., Fan, H., Jin, J., Botella, M.A., Jiang, L., and Lin, J.
1020 (2011). Golgi apparatus-localized synaptotagmin 2 is required for
1021 unconventional secretion in Arabidopsis. PLoS ONE 6: e26477.
1022

1023 **Figure Legends**

1024 **Figure 1. *Sec23* and *Sec24* are required for polarized growth.** Gene models of
1025 the *P. patens Sec23* (A) and *Sec24* (B) genes are shown with exons indicated by
1026 boxes and introns by thin black lines. Coding and untranslated regions are
1027 denoted by thick and thin boxes, respectively. The lines underneath the gene
1028 models represent sequence regions targeted by RNAi constructs. Scale bar is
1029 500bp. Graphs depict the relative expression of *Sec23* and *Sec24* genes
1030 normalized to UBIQUITIN10 in 8-day-old wild-type moss plants regenerated
1031 from protoplasts. N = 3, Error bars are s.e.m. (C, E) Representative chlorophyll
1032 autofluorescence images of 7-day-old plants regenerated from protoplasts

1033 expressing the indicated RNAi constructs. Scale bar, 100 μm. (D, F)
1034 Quantification of plant area is based on the area of the chlorophyll
1035 autofluorescence and is presented normalized to the area of the control for each
1036 experiment. Means are indicated by horizontal lines. Letters indicate groups with
1037 significantly different means as determined by a one-way ANOVA with a Tukey
1038 *post hoc* test (α=0.05).
1039
1040 **Figure 2. *Sec23D* and *Sec23E* are functionally redundant.** (A) *Sec23D* and
1041 *Sec23E* gene models are shown with exons indicated by boxes and introns by
1042 thin black lines. Coding and untranslated regions are denoted by thick and thin
1043 boxes, respectively. The lines underneath the gene models represent sequence
1044 regions that were targeted by *Sec23D* or *Sec23E* UTR RNAi constructs. Scale bar
1045 is 500bp. (B) Representative chlorophyll autofluorescence images of 7-day-old
1046 plants regenerated from protoplasts expressing the indicated constructs. Scale
1047 bar, 100 μm. (C) Quantification of plant area was normalized to the control for
1048 each experiment. Letters indicate groups with significantly different means as
1049 determined by a one-way ANOVA with a Tukey *post hoc* test (α=0.05).
1050
1051 **Figure 3. CRISPR-Cas9-mediated deletion of *Sec23* isoforms demonstrates**
1052 **that *Sec23D* is critical for protonemal growth.** (A) Representative chlorophyll
1053 autofluorescence images of 7-day old plants with the indicated genotype
1054 regenerated from protoplasts. Scale bar, 100μm. (B) Quantification of plant area
1055 normalized to the wild type control. (C) Representative 3-week old moss plants
1056 with the indicated genotype. Scale bar, 1mm. (D) Quantification of the plant area
1057 of 3-week old moss plants normalized to that of the wild type control. (E)
1058 Number of gametophores in 3-week old moss plants. Letters in (B, D-E) indicate
1059 groups with significantly different means as determined by a one-way ANOVA
1060 with a Tukey *post hoc* test (α=0.05). (F) Relative expression of *Sec23D* and *E*
1061 genes normalized to UBIQUITIN10 in 8-day-old wild type and *Δsec23abcfg-1*, and
1062 *Δsec23abcfg-2* moss plants regenerated from protoplasts. N=3, Error bars are
1063 s.e.m. No significant difference was determined by a one-way ANOVA with a
1064 Tukey *post hoc* test (α=0.05).
1065

1066 **Figure 4. Loss of Sec23D causes ER morphology defects and ER stress.** (A)
1067 Laser scanning confocal images of the ER labeled with GFP-KDEL in the indicated
1068 genotype. Colored boxes highlight large and small ER aggregates found in the
1069 *Δsec23d-B11* mutant. Scale bars, 5 μm. (B) Spinning disc confocal super
1070 resolution imaging of the ER labeled with GFP-KDEL in a *Δsec23d-B11* cell. Scale
1071 bar, 5 μm. Box outlined with yellow dotted line is enlarged to the right and the
1072 box outlined with a white dotted line is enlarged below with optical sections
1073 spaced every 0.5 μm shown for this region of the cell. Scale bars in boxed
1074 regions, 2 μm. Also see Movie S1. (C, D) Relative expression of *PpBip1* in 8-day
1075 old moss plants regenerated from protoplasts. N=3, Error bars are s.e.m.
1076 Asterisks denote t-probability is <0.01. n.s. denotes no significant difference. In
1077 (B) BFA-treated plants were normalized to DMSO-treated plants and in (C) null
1078 mutants were normalized to wild type plants.
1079
1080 **Figure 5. Deletion of *Sec23D* inhibits Golgi trafficking and secretion to the**
1081 **plasma membrane.** (A) Representative maximum projections of confocal
1082 images of the indicated genotypes expressing a YFP-MAN marker. Scale bar, 10
1083 μm. (B) Quantification of the fluorescence intensity ratio within the Golgi to the
1084 background. (C) Representative medial sections of confocal images of the
1085 indicated genotypes expressing a plasma membrane marker (FSnap-mCherry).
1086 Scale bar, 10 μm. (D) Quantification of the fluorescence intensity ratio of the
1087 plasma membrane to the intensity within the cell. Letters in (B, D) indicate
1088 groups with significantly different means as determined by a one-way ANOVA
1089 with a Tukey *post hoc* test (α=0.05).
1090
1091 **Figure 6. Sec23 isoforms localize to ER proximal structures with distinct**
1092 **sizes.** (A) Representative confocal Z-sections of lines where the indicated Sec23
1093 gene was endogenously tagged with 3XmRuby in a line that expresses GFP-KDEL
1094 labeling the ER lumen (ER-GFP). Scale bars, 5 μm. Boxed region in the mRuby
1095 channel is shown to the right of each image. (B) Pearson's correlation coefficient
1096 measured between the Sec23 labeled lines and ER-GFP. O, original ER image; V,
1097 vertically flipped ER image; H, horizontally flipped ER image. Asterisks denote
1098 p<0.001as determined by a one-way ANOVA with a Tukey *post hoc* test (α=0.05)

1099 (C) Representative confocal Z-sections of *Sec23* genes endogenously tagged with
1100 3XmRuby acquired with the optimal resolution of the confocal imaging system.
1101 Scale bars, 5 μm. (D) Quantification of average dot size in the Sec23 images as
1102 determined by the diAna tool for Fiji (Gilles et al., 2017). Asterisks denote
1103 $p<0.001$ as determined by a one-way ANOVA with a Tukey *post hoc* test ($\alpha=0.05$).
1104
1105 **Figure 7. Sec23B and Sec23G form ER exit sites independent of Sec23D.**
1106 Representative confocal Z-sections of Sec23D-mRuby lines where Sec23B (A) or
1107 Sec23G (B) were endogenously tagged with mNeon. Scale bar, 5 μm. Yellow
1108 boxed regions are enlarged to the right of the merged image where Sec23D-
1109 mRuby is false-colored magenta and in (A) Sec23B-mNeon is false-colored green
1110 and in (B) Sec23G-mNeon is false-colored green. (C) Percent of Sec23B-mNeon
1111 or Sec23G-mNeon dots that co-localized with Sec23D-mRuby and (D) center-to-
1112 center distance of co-localized particles as determined using the diAna tool for
1113 Fiji (Gilles et al., 2017). (E) Representative confocal Z-sections of wild type and
1114 *Δsec23d-5* cells with either Sec23B or Sec23G endogenously tagged with
1115 3XmRuby. Scale bar, 5 μm. (F) Quantification of average dot size as determined
1116 by the diAna tool for Fiji (Gilles et al., 2017). Sec23B and Sec23G dot size in wild
1117 type is the same data presented in Figure 6D. Student t-test was performed for
1118 data in (C, D, and F). The t-probability is indicated for each data pair in each
1119 graph. n.s. denotes no significant difference.

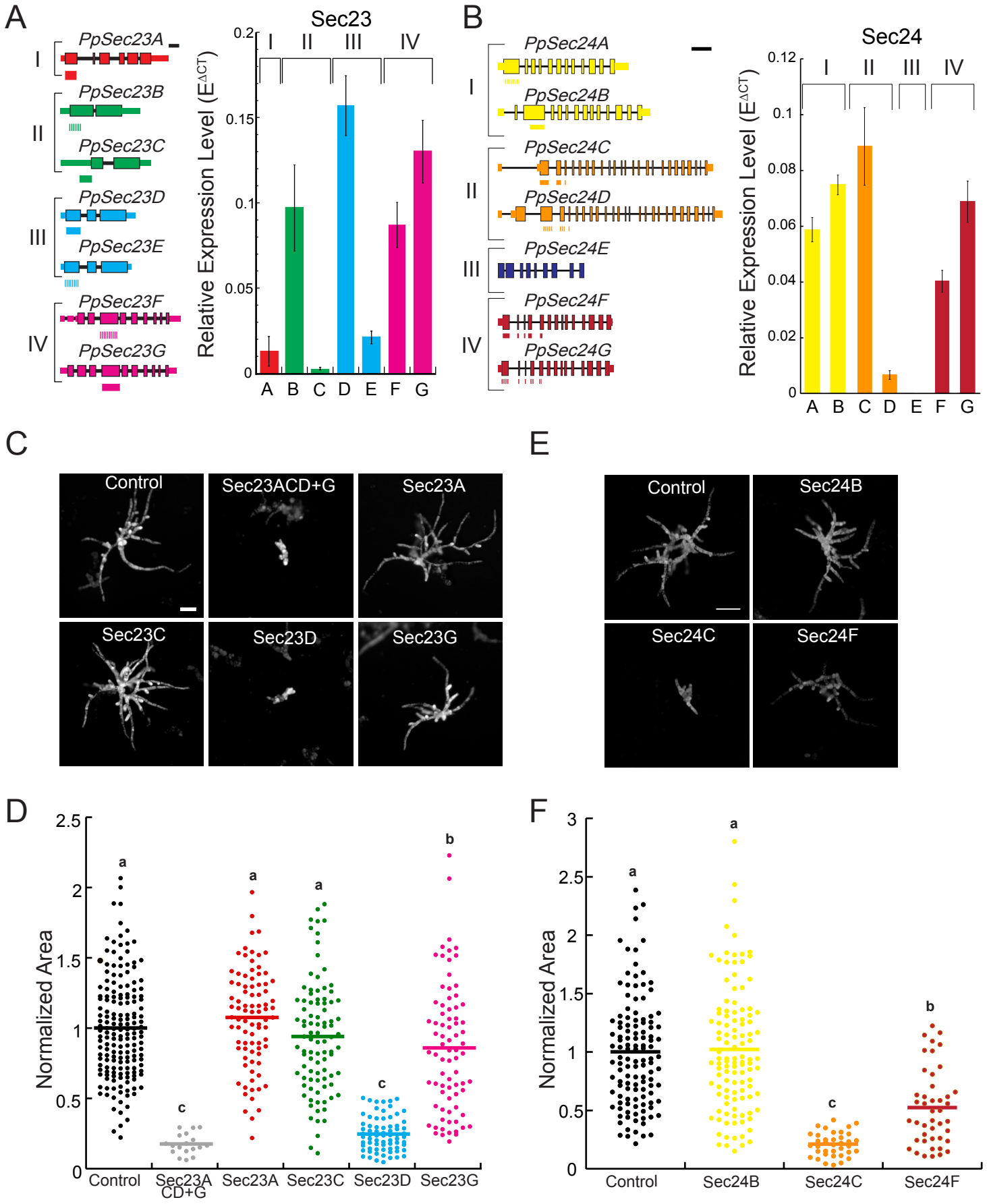
A
PpSec23A
PpSec23B
PpSec23C
PpSec23D
PpSec23E
PpSec23F
PpSec23G
I
II
III
IV
Sec23
Relative Expression Level (E^ΔCT)
0.2
0.15
0.1
0.05
0
A B C D E F G
B
PpSec24A
PpSec24B
PpSec24C
PpSec24D
PpSec24E
PpSec24F
PpSec24G
Sec24
0.12
0.1
0.08
0.06
0.04
0.02
C
Control
Sec23ACD+G
Sec23A
Sec23C
Sec23D
Sec23G
E
Control
Sec24B
Sec24C
Sec24F
D
Normalized Area
2.5
2
1.5
1
0.5
0
a
c
b
Control
Sec23A CD+G
Sec23A
Sec23C
Sec23D
Sec23G
F
3
Sec24B
Sec24C
Sec24F

Figure 1. *Sec23* and *Sec24* are required for polarized growth. Gene models of the *P. patens Sec23* (A) and *Sec24* (B) genes are shown with exons indicated by boxes and introns by thin black lines. Coding and untranslated regions are denoted by thick and thin boxes, respectively. The lines underneath the gene models represent sequence regions targeted by RNAi constructs. Scale bar is 500bp. Graphs depict the relative expression of *Sec23* and *Sec24* genes normalized to UBIQUITIN10 in 8-day-old wild-type moss plants regenerated from protoplasts. N = 3, Error bars are s.e.m. (C, E) Representative chlorophyll autofluorescence images of 7-day-old plants regenerated from protoplasts expressing the indicated RNAi constructs. Scale bar, 100 µm. (D, F) Quantification of plant area is based on the area of the chlorophyll autofluorescence and is presented normalized to the area of the control for each experiment. Means are indicated by horizontal lines. Letters indicate groups with significantly different means as determined by a one-way ANOVA with a Tukey *post hoc* test (α=0.05).

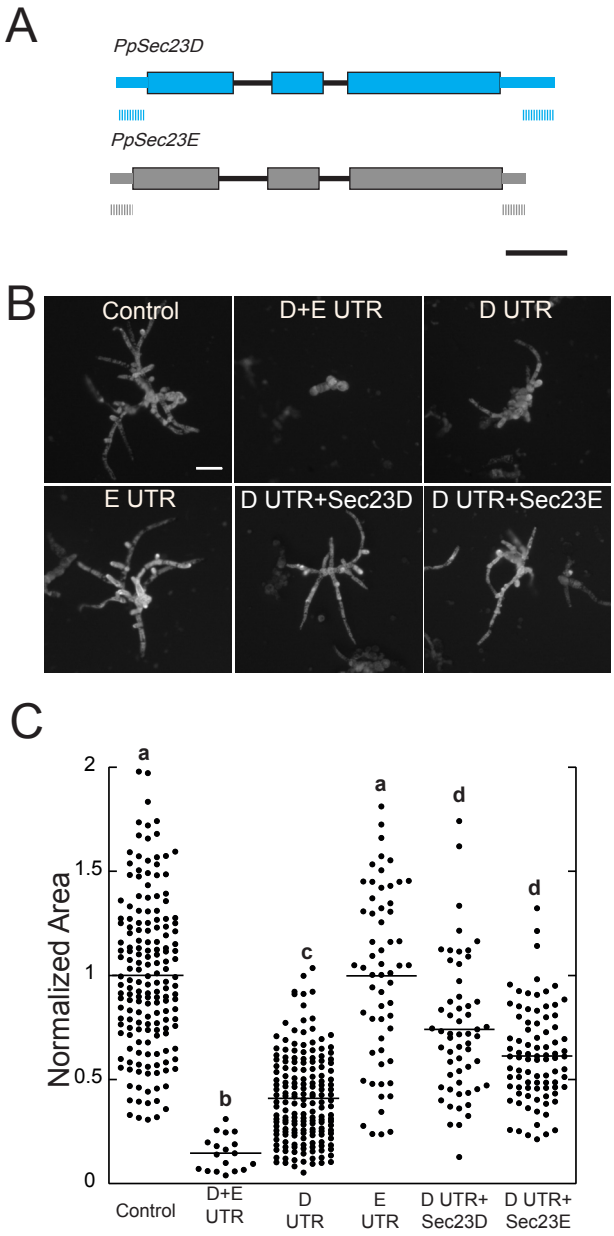

Figure 2. *Sec23D* and *Sec23E* are functionally redundant. (A) *Sec23D* and *Sec23E* gene models are shown with exons indicated by boxes and introns by thin black lines. Coding and untranslated regions are denoted by thick and thin boxes, respectively. The lines underneath the gene models represent sequence regions that were targeted by *Sec23D* or *Sec23E* UTR RNAi constructs. Scale bar is 500bp. (B) Representative chlorophyll autofluorescence images of 7-day-old plants regenerated from protoplasts expressing the indicated constructs. Scale bar, 100 µm. (C) Quantification of plant area was normalized to the control for each experiment. Letters indicate groups with significantly different means as determined by a one-way ANOVA with a Tukey *post hoc* test (α=0.05).

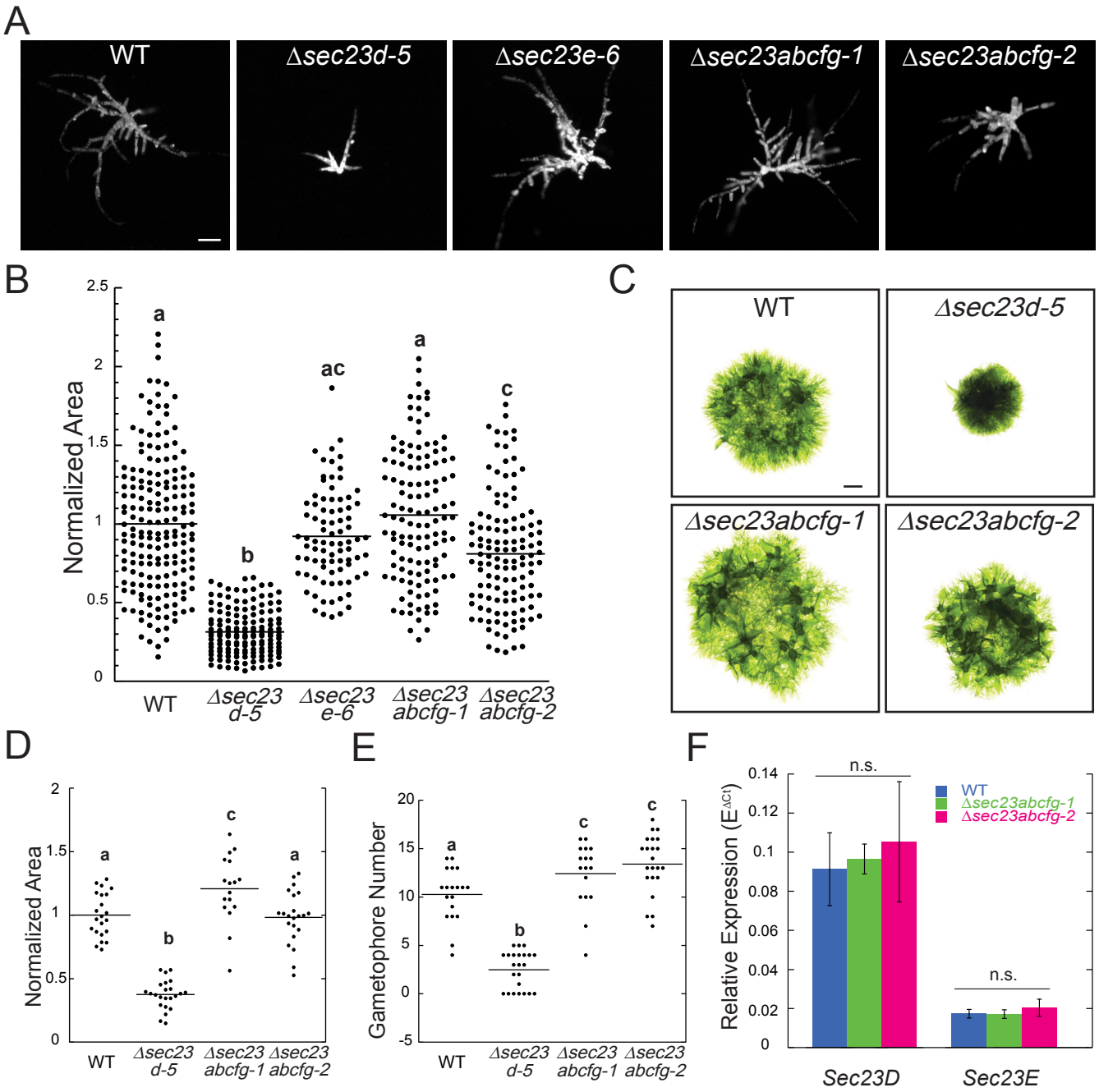

Figure 3. CRISPR-Cas9-mediated deletion of *Sec23* isoforms demonstrates that *Sec23D* is critical for protonemal growth. (A) Representative chlorophyll autofluorescence images of 7-day old plants with the indicated genotype regenerated from protoplasts. Scale bar, 100µm. (B) Quantification of plant area normalized to the wild type control. (C) Representative 3-week old moss plants with the indicated genotype. Scale bar, 1mm. (D) Quantification of the plant area of 3-week old moss plants normalized to that of the wild type control. (E) Number of gametophores in 3-week old moss plants. Letters in (B, D-E) indicate groups with significantly different means as determined by a one-way ANOVA with a Tukey *post hoc* test (α=0.05). (F) Relative expression of *Sec23D* and *E* genes normalized to UBIQUITIN10 in 8-day-old wild type and Δ*sec23abcfg-1*, and Δ*sec23abcfg-2* moss plants regenerated from protoplasts. N=3, Error bars are s.e.m. No significant difference was determined by a one-way ANOVA with a Tukey *post hoc* test (α=0.05).

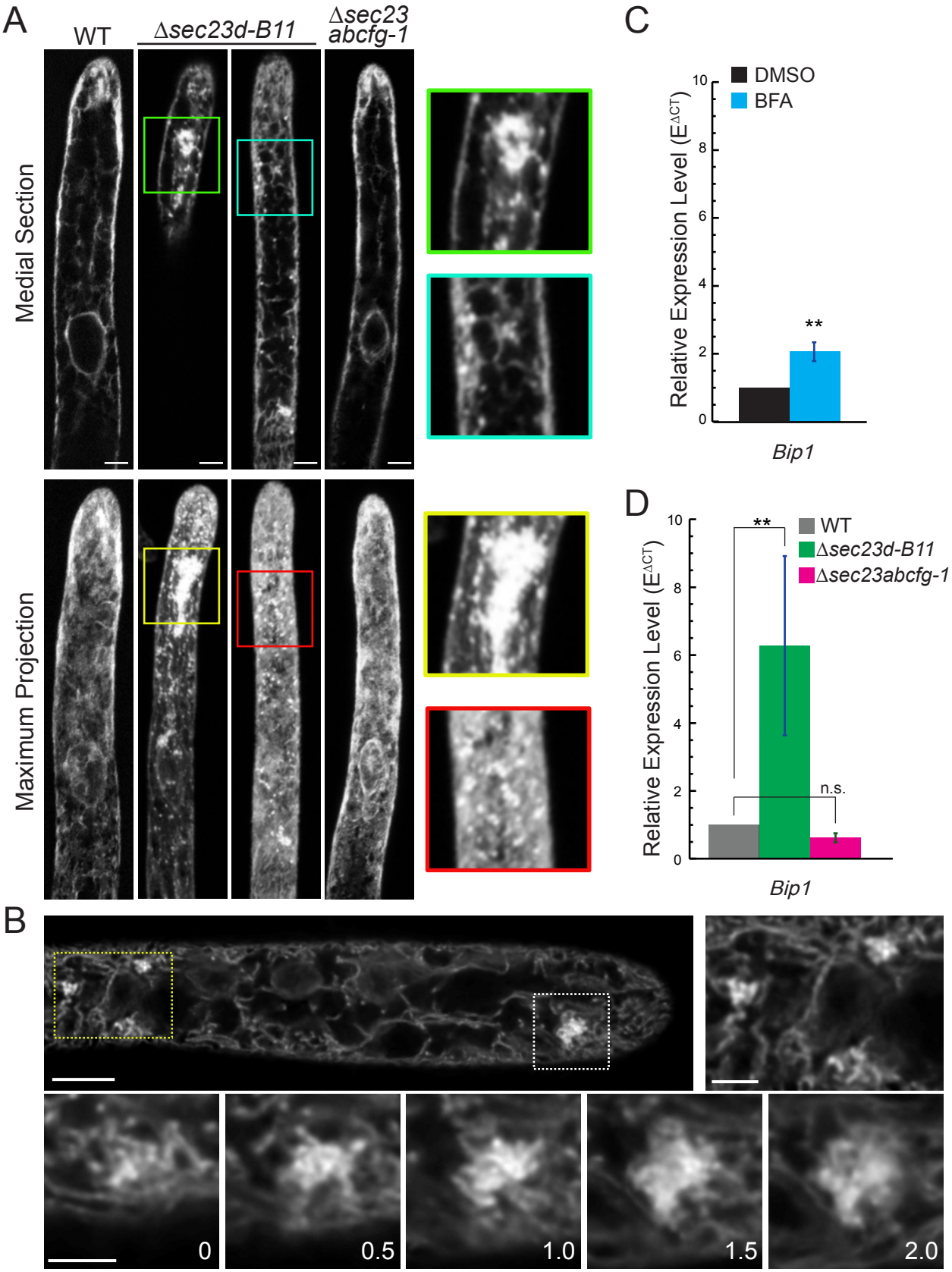

Figure 4. Loss of Sec23D causes ER morphology defects and ER stress. (A) Laser scanning confocal images of the ER labeled with GFP-KDEL in the indicated genotype. Colored boxes highlight large and small ER aggregates found in the Δ*sec23d-B11* mutant. Scale bars, 5 µm. (B) Spinning disc confocal super resolution imaging of the ER labeled with GFP-KDEL in a Δ*sec23d-B11* cell. Scale bar, 5 µm. Box outlined with yellow dotted line is enlarged to the right and the box outlined with a white dotted line is enlarged below with optical sections spaced every 0.5 µm shown for this region of the cell. Scale bars in boxed regions, 2 µm. Also see Movie S1. (C, D) Relative expression of *PpBip1* in 8-day old moss plants regenerated from protoplasts. N=3, Error bars are s.e.m. Asterisks denote t-probability is <0.01. n.s. denotes no significant difference. In (B) BFA-treated plants were normalized to DMSO-treated plants and in (C) null mutants were normalized to wild type plants.

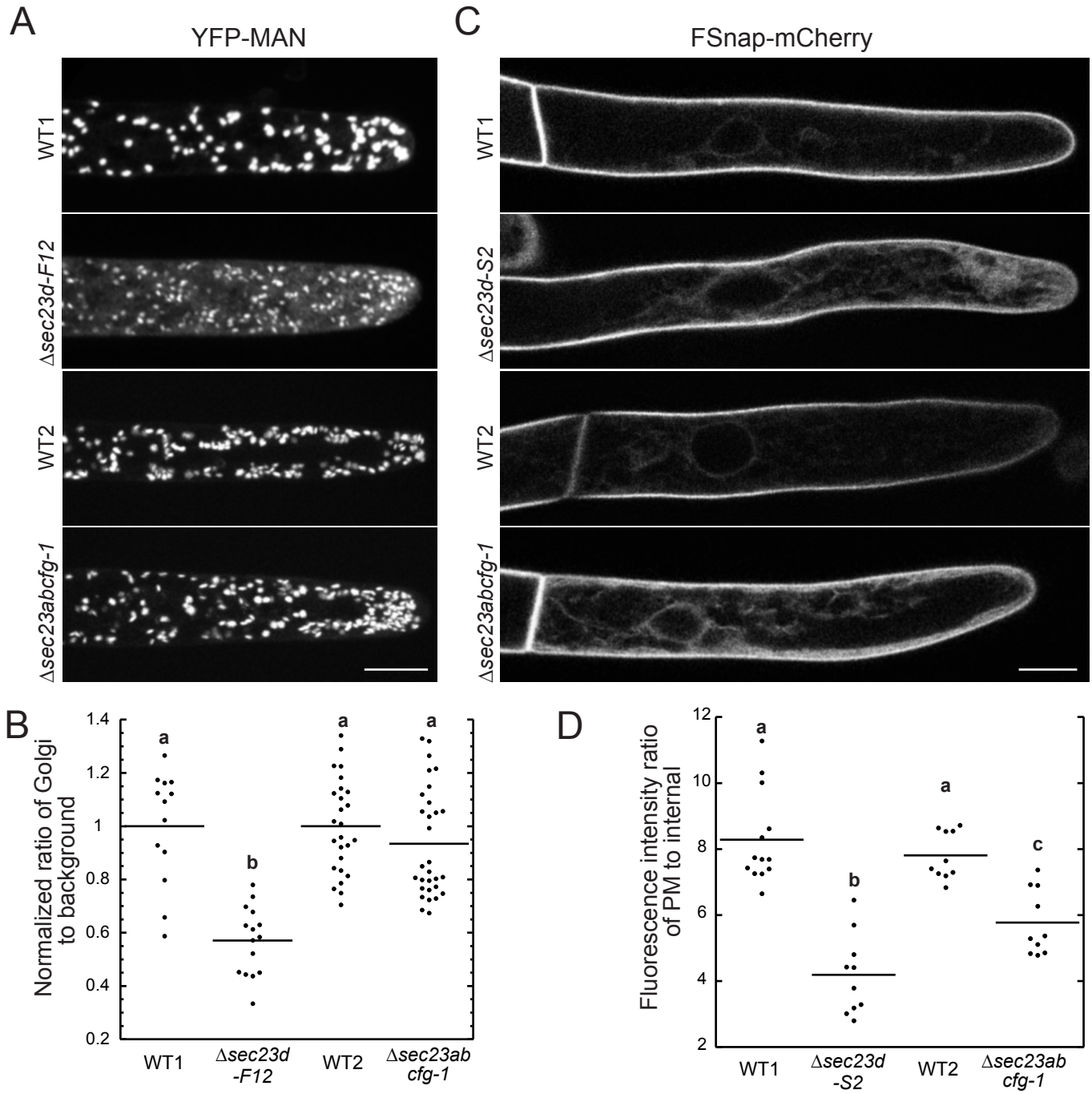

Figure 5. Deletion of *Sec23D* inhibits Golgi trafficking and secretion to the plasma membrane. (A) Representative maximum projections of confocal images of the indicated genotypes expressing a YFP-MAN marker. Scale bar, 10 μm. (B) Quantification of the fluorescence intensity ratio within the Golgi to the background. (C) Representative medial sections of confocal images of the indicated genotypes expressing a plasma membrane marker (FSnap-mCherry). Scale bar, 10 μm. (D) Quantification of the fluorescence intensity ratio of the plasma membrane to the intensity within the cell. Letters in (B, D) indicate groups with significantly different means as determined by a one-way ANOVA with a Tukey *post hoc* test (α=0.05).

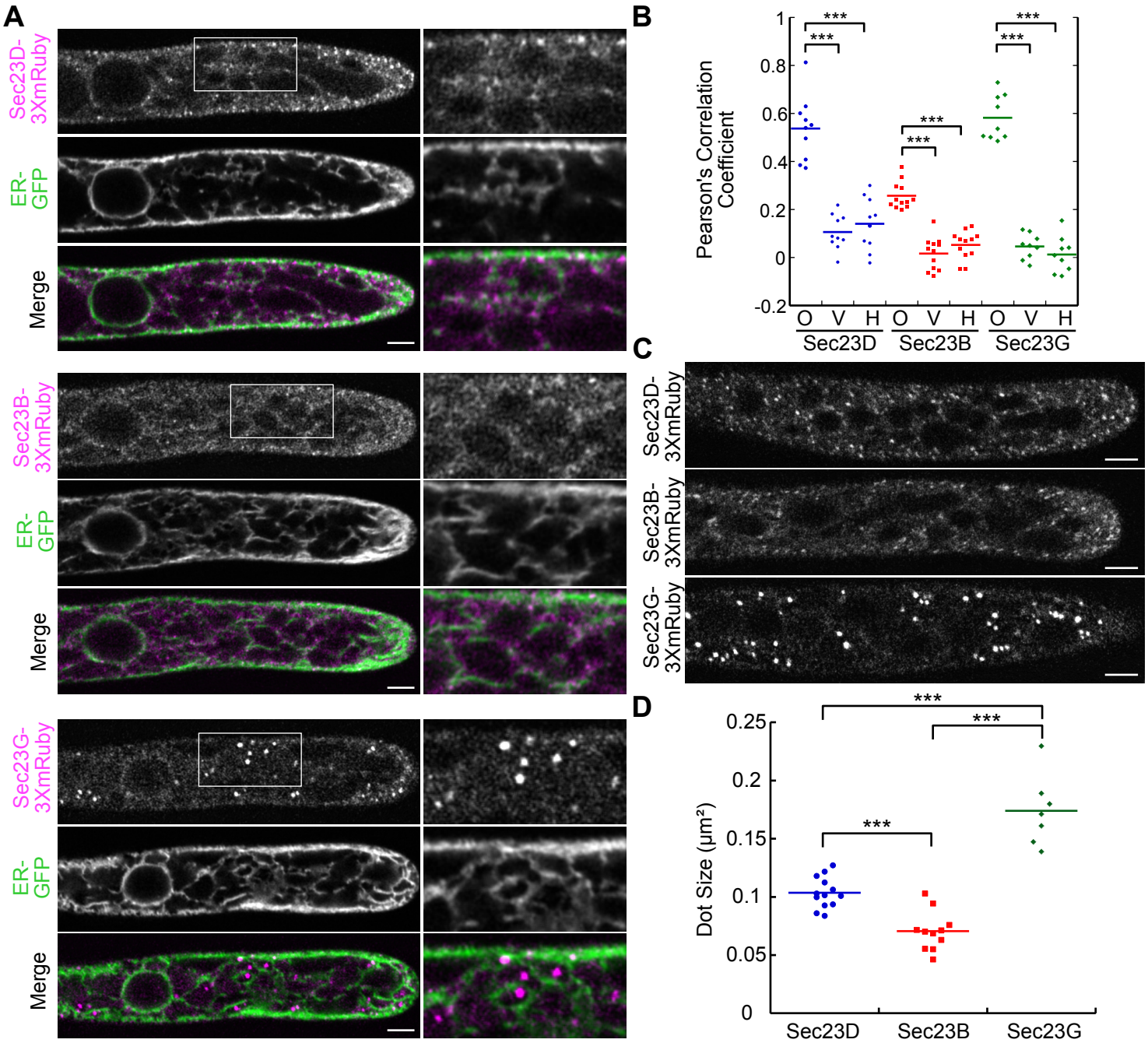

Figure 6. Sec23 isoforms localize to ER proximal structures with distinct sizes. (A) Representative confocal Z-sections of lines where the indicated Sec23 gene was endogenously tagged with 3XmRuby in a line that expresses GFP-KDEL labeling the ER lumen (ER-GFP). Scale bars, 5 µm. Boxed region in the mRuby channel is shown to the right of each image. (B) Pearson's correlation coefficient measured between the Sec23 labeled lines and ER-GFP. O, original ER image; V, vertically flipped ER image; H, horizontally flipped ER image. Asterisks denote p<0.001as determined by a one-way ANOVA with a Tukey *post hoc* test (α=0.05) (C) Representative confocal Z-sections of *Sec23* genes endogenously tagged with 3XmRuby acquired with the optimal resolution of the confocal imaging system. Scale bars, 5 µm. (D) Quantification of average dot size in the Sec23 images as determined by the diAna tool for Fiji (Gilles et al., 2017). Asterisks denote p<0.001 as determined by a one-way ANOVA with a Tukey *post hoc* test (α=0.05).

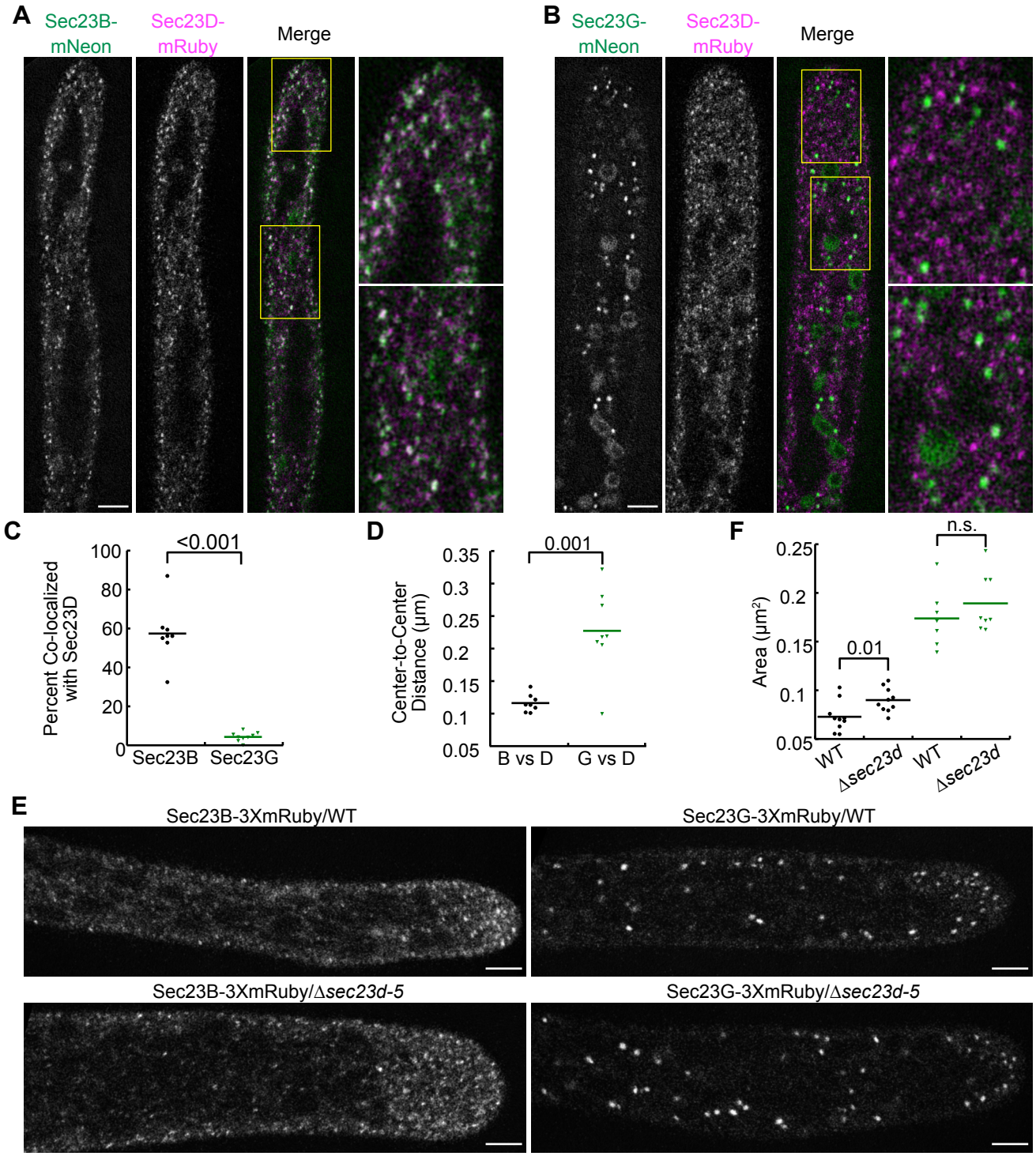

Figure 7. Sec23B and Sec23G form ER exit sites independent of Sec23D. Representative confocal Z-sections of Sec23D-mRuby lines where Sec23B (A) or Sec23G (B) were endogenously tagged with mNeon. Scale bar, 5 µm. Yellow boxed regions are enlarged to the right of the merged image where Sec23D-mRuby is false-colored magenta and in (A) Sec23B-mNeon is false-colored green and in (B) Sec23G-mNeon is false-colored green. (C) Percent of Sec23B-mNeon or Sec23G-mNeon dots that co-localized with Sec23D-mRuby and (D) center-to-center distance of co-localized particles as determined using the diAna tool for Fiji (Gilles et al., 2017). (E) Representative confocal Z-sections of wild type and Δ*sec23d-5* cells with either Sec23B or Sec23G endogenously tagged with 3XmRuby. Scale bar, 5 µm. (F) Quantification of average dot size as determined by the diAna tool for Fiji (Gilles et al., 2017). Sec23B and Sec23G dot size in wild type is the same data presented in Figure 6D. Student t-test was performed for data in (C, D, and F). The t-probability is indicated for each data pair in each graph. n.s. denotes no significant difference.

Parsed Citations

Aridor, M. (2018). COPII gets in shape: Lessons derived from morphological aspects of early secretion. Traffic 19: 823–839.
Google Scholar: Author Only Title Only Author and Title

Aridor, M., Fish, K.N., Bannykh, S., Weissman, J., Roberts, T.H., Lippincott-Schwartz, J., and Balch, W.E. (2001). The Sar1 Gtpase Coordinates Biosynthetic Cargo Selection with Endoplasmic Reticulum Export Site Assembly. Journal of Cell Biology 152: 213–230.
Google Scholar: Author Only Title Only Author and Title

Aridor, M., Weissman, J., Bannykh, S., Nuoffer, C., and Balch, W.E. (1998). Cargo Selection by the COPII Budding Machinery during Export from the ER. Journal of Cell Biology 141: 61–70.
Google Scholar: Author Only Title Only Author and Title

Augustine, R.C., Pattavina, K.A., Tüzel, E., Vidali, L., and Bezanilla, M. (2011). Actin interacting protein1 and actin depolymerizing factor drive rapid actin dynamics in Physcomitrella patens. Plant Cell 23: 3696–3710.
Google Scholar: Author Only Title Only Author and Title

Barlow, L.D. and Dacks, J.B. (2018). Seeing the endomembrane system for the trees: Evolutionary analysis highlights the importance of plants as models for eukaryotic membrane-trafficking. Seminars in Cell & Developmental Biology 80: 142–152.
Google Scholar: Author Only Title Only Author and Title

Barlowe, C. (2003). Signals for COPII-dependent export from the ER: what's the ticket out? Trends in Cell Biology 13: 295–300.
Google Scholar: Author Only Title Only Author and Title

Barlowe, C. and Helenius, A. (2016). Cargo Capture and Bulk Flow in the Early Secretory Pathway. Annu. Rev. Cell Dev. Biol. 32: 197–222.
Google Scholar: Author Only Title Only Author and Title

Barlowe, C. and Schekman, R. (1993). SEC12 encodes a guanine-nucleotide-exchange factor essential for transport vesicle budding from the ER. Nature 365: 347–349.
Google Scholar: Author Only Title Only Author and Title

Bascom, C.S., Wu, S.-Z., Nelson, K., Oakey, J., and Bezanilla, M. (2016). Long-Term Growth of Moss in Microfluidic Devices Enables Subcellular Studies in Development. Plant Physiology 172: 28–37.
Google Scholar: Author Only Title Only Author and Title

Belden, W.J. (2001). Role of Erv29p in Collecting Soluble Secretory Proteins into ER-Derived Transport Vesicles. Science 294: 1528–1531.
Google Scholar: Author Only Title Only Author and Title

Bezanilla, M., Perroud, P.-F., Pan, A., Klueh, P., and Quatrano, R.S. (2005). An RNAi system in Physcomitrella patens with an internal marker for silencing allows for rapid identification of loss of function phenotypes. Plant Biol (Stuttg) 7: 251–257.
Google Scholar: Author Only Title Only Author and Title

Bi, X., Corpina, R.A., and Goldberg, J. (2002). Structure of the Sec23/24–Sar1 pre-budding complex of the COPII vesicle coat. Nature 419: 271–277.
Google Scholar: Author Only Title Only Author and Title

Brandizzi, F. (2018). Transport from the endoplasmic reticulum to the Golgi in plants: Where are we now? Seminars in Cell & Developmental Biology 80: 94–105.
Google Scholar: Author Only Title Only Author and Title

Brandizzi, F. and Barlowe, C. (2013). Organization of the ER–Golgi interface for membrane traffic control. Nat Rev Mol Cell Biol 14: 382–392.
Google Scholar: Author Only Title Only Author and Title

Cheng, F-y., Zamski, E., Guo W-w., Mason Pharr, D., and Williamson, J.D. (2009). Salicylic acid stimulates secretion of the normally symplastic enzyme mannitol dehydrogenase: a possible defense against mannitol-secreting fungal pathogens. Planta 230: 1093–1103.
Google Scholar: Author Only Title Only Author and Title

Cheng, X., and Bezanilla M. (2021). SABRE populates ER domains essential for cell plate maturation and cell expansion influencing cell and tissue patterning. eLife 10: e65166.
Google Scholar: Author Only Title Only Author and Title

Cho, Y. and Kanehara, K. (2017). Endoplasmic Reticulum Stress Response in Arabidopsis Roots. Front. Plant Sci. 8.
Google Scholar: Author Only Title Only Author and Title

Chung, K.P., Zeng, Y., and Jiang, L. (2016). COPII Paralogs in Plants: Functional Redundancy or Diversity? Trends in Plant Science 21: 758–769.
Google Scholar: Author Only Title Only Author and Title

De Craene, J.-O., Courte, F., Rinaldi, B., Fitterer, C., Herranz, M.C., Schmitt-Keichinger, C., Ritzenthaler, C., and Friant, S. (2014). Study of the Plant COPII Vesicle Coat Subunits by Functional Complementation of Yeast Saccharomyces cerevisiae Mutants. PLoS ONE 9:

e90072.
Google Scholar: Author Only Title Only Author and Title

Ding, Y., Wang, J., Wang, J., Stierhof, Y-D., Robinson, D.G., and Jiang L. (2012). Unconventional protein secretion. Trends in Plant Science 17: 606-615.
Google Scholar: Author Only Title Only Author and Title

Faso, C., Chen, Y.-N., Tamura, K., Held, M., Zemelis, S., Marti, L., Saravanan, R., Hummel, E., Kung, L., Miller, E., Hawes, C., and Brandizzi, F. (2009). A Missense Mutation in the Arabidopsis COPII Coat Protein Sec24A Induces the Formation of Clusters of the Endoplasmic Reticulum and Golgi Apparatus. The Plant Cell 21: 3655–3671.
Google Scholar: Author Only Title Only Author and Title

Fath, S., Mancias, J.D., Bi, X., and Goldberg, J. (2007). Structure and Organization of Coat Proteins in the COPII Cage. Cell 129: 1325–1336.
Google Scholar: Author Only Title Only Author and Title

Furt, F., Lemoi, K., Tüzel, E., and Vidali, L. (2012). Quantitative analysis of organelle distribution and dynamics in Physcomitrella patens protonemal cells. BMC Plant Biol. 12: 70.
Google Scholar: Author Only Title Only Author and Title

Galotto, G., Bibeau, J.P., and Vidali, L. (2019). Automated Image Acquisition and Morphological Analysis of Cell Growth Mutants in Physcomitrella patens. In Plant Cell Morphogenesis, F. Cvrčková and V. Žárský, eds, Methods in Molecular Biology. (Springer New York: New York, NY), pp. 307–322.
Google Scholar: Author Only Title Only Author and Title

Gilles, J.-F., Dos Santos, M., Boudier, T., Bolte, S., and Heck, N. (2017). DiAna, an ImageJ tool for object-based 3D co-localization and distance analysis. Methods 115: 55–64.
Google Scholar: Author Only Title Only Author and Title

Giraudo, C.G. and Maccioni, H.J.F. (2003). Endoplasmic Reticulum Export of Glycosyltransferases Depends on Interaction of a Cytoplasmic Dibasic Motif with Sar1. MBoC 14: 3753–3766.
Google Scholar: Author Only Title Only Author and Title

van Gisbergen, P.A.C., Wu, S.-Z., Chang, M., Pattavina, K.A., Bartlett, M.E., and Bezanilla, M. (2018). An ancient Sec10-formin fusion provides insights into actin-mediated regulation of exocytosis. J. Cell Biol. 217: 945–957.
Google Scholar: Author Only Title Only Author and Title

Haeussler, M., Schönig, K., Eckert, H., Eschstruth, A., Mianné, J., Renaud, J.-B., Schneider-Maunoury, S., Shkumatava, A., Teboul, L., Kent, J., Joly, J.-S., and Concordet, J.-P. (2016). Evaluation of off-target and on-target scoring algorithms and integration into the guide RNA selection tool CRISPOR. Genome Biol. 17: 148.
Google Scholar: Author Only Title Only Author and Title

Hanna, M.G., Peotter, J.L., Frankel, E.B., and Audhya, A. (2018). Membrane Transport at an Organelle Interface in the Early Secretory Pathway: Take Your Coat Off and Stay a While: Evolution of the metazoan early secretory pathway. BioEssays 40: 1800004.
Google Scholar: Author Only Title Only Author and Title

Hanton, S.L., Matheson, L.A., Chatre, L., and Brandizzi, F. (2009). Dynamic organization of COPII coat proteins at endoplasmic reticulum export sites in plant cells. The Plant Journal 57: 963–974.
Google Scholar: Author Only Title Only Author and Title

Heinze, L., Freimuth, N., Rößling, A.-K., Hahnke, R., Riebschläger, S., Fröhlich, A., Sampathkumar, A., McFarlane, H.E., and Sauer, M. (2020). EPSIN1 and MTV1 define functionally overlapping but molecularly distinct trans-Golgi network subdomains in Arabidopsis. PNAS 117: 25880–25889.
Google Scholar: Author Only Title Only Author and Title

Hino, T., Tanaka, Y., Kawamukai, M., Nishimura, K., Mano, S., and Nakagawa, T. (2011). Two Sec13p Homologs, AtSec13A and AtSec13B, Redundantly Contribute to the Formation of COPII Transport Vesicles in Arabidopsis thaliana. Bioscience, Biotechnology, and Biochemistry 75: 1848–1852.
Google Scholar: Author Only Title Only Author and Title

Hiwatashi, Y., Sato, Y., and Doonan, J.H. (2014). Kinesins Have a Dual Function in Organizing Microtubules during Both Tip Growth and Cytokinesis in Physcomitrella patens. The Plant Cell 26: 1256–1266.
Google Scholar: Author Only Title Only Author and Title

Jensen, D. and Schekman, R. (2011). COPII-mediated vesicle formation at a glance. Journal of Cell Science 124: 1–4.
Google Scholar: Author Only Title Only Author and Title

Khoriaty, R. et al. (2018). Functions of the COPII gene paralogs SEC23A and SEC23B are interchangeable in vivo. Proc Natl Acad Sci USA 115: E7748–E7757.
Google Scholar: Author Only Title Only Author and Title

Lee, M.H., Lee, S.H., Kim, H., Jin, J.B., Kim, D.H., and Hwang, I. A WD40 Repeat Protein, Arabidopsis Sec13 Homolog 1, May Play a Role in Vacuolar Trafficking by Controlling the Membrane Association of AtDRP2A: 10.

Mallett, D.R., Chang, M., Cheng, X., and Bezanilla, M. (2019). Efficient and modular CRISPR-Cas9 vector system for Physcomitrella patens. Plant Direct 3: e00168-15.
Google Scholar: Author Only Title Only Author and Title

Mancias, J.D. and Goldberg, J. (2007). The Transport Signal on Sec22 for Packaging into COPII-Coated Vesicles Is a Conformational Epitope. Molecular Cell 26: 403–414.
Google Scholar: Author Only Title Only Author and Title

Maruyama, D., Sugiyama, T., Endo, T., and Nishikawa, S. (2014). Multiple BiP Genes of Arabidopsis thaliana are Required for Male Gametogenesis and Pollen Competitiveness. Plant and Cell Physiology 55: 801–810.
Google Scholar: Author Only Title Only Author and Title

Mossessova, E., Bickford, L.C., and Goldberg, J. (2003). SNARE selectivity of the COPII coat. Cell 114: 483–495.
Google Scholar: Author Only Title Only Author and Title

Nakano, A. and Muramatsu, M. (1989). A Novel GTP-binding Protein, Sar1p, Is Involved in Transport from the Endoplasmic Reticulum to the Golgi Apparatus. The Journal of Cell Biology 109: 2677–2691.
Google Scholar: Author Only Title Only Author and Title

Nakano, R.T., Matsushima, R., Ueda, H., Tamura, K., Shimada, T., Li, L., Hayashi, Y., Kondo, M., Nishimura, M., and Hara-Nishimura, I. (2009). GNOM-LIKE1/ERMO1 and SEC24a/ERMO2 Are Required for Maintenance of Endoplasmic Reticulum Morphology in Arabidopsis thaliana. The Plant Cell 21: 3672–3685.
Google Scholar: Author Only Title Only Author and Title

Nebenfuhr, A. (2002). Brefeldin A: Deciphering an Enigmatic Inhibitor of Secretion. Plant physiology 130: 1102–1108.
Google Scholar: Author Only Title Only Author and Title

Nelson, B.K., Cai, X., and Nebenführ, A. (2007). A multicolored set of in vivo organelle markers for co-localization studies in Arabidopsis and other plants. Plant J. 51: 1126–1136.
Google Scholar: Author Only Title Only Author and Title

Niu, T.-K., Pfeifer, A.C., Lippincott-Schwartz, J., and Jackson, C.L. (2005). Dynamics of GBF1, a Brefeldin A-Sensitive Arf1 Exchange Factor at the Golgi□V. Molecular Biology of the Cell 16: 1213–1222.
Google Scholar: Author Only Title Only Author and Title

Noh, S.-J., Kwon, C.S., Oh, D.-H., Moon, J.S., and Chung, W.-I. (2003). Expression of an evolutionarily distinct novel BiP gene during the unfolded protein response in Arabidopsis thaliana. Gene 311: 81–91.
Google Scholar: Author Only Title Only Author and Title

Novick, P., Field, C., and Schekman, R. (1980). Identification of 23 complementation groups required for post-translational events in the yeast secretory pathway. Cell 21: 205–215.
Google Scholar: Author Only Title Only Author and Title

Nufer, O. (2003). ER export of ERGIC-53 is controlled by cooperation of targeting determinants in all three of its domains. Journal of Cell Science 116: 4429–4440.
Google Scholar: Author Only Title Only Author and Title

Ortiz-Ramírez, C., Michard, E., Simon, A.A., Damineli, D.S.C., Hernandez-Coronado, M., Becker, J.D., and Feijó, J.A. (2017). GLUTAMATE RECEPTOR-LIKE channels are essential for chemotaxis and reproduction in mosses. Nature 549: 91–95.
Google Scholar: Author Only Title Only Author and Title

Qu, X., Zhang, R., Zhang, M., Diao, M., Xue, Y., and Huang, S. (2017). Organizational innovation of apical actin filaments drives rapid pollen tube growth and turning. Mol Plant 10: 930–947.
Google Scholar: Author Only Title Only Author and Title

Rensing, S.A., Goffinet, B., Meyberg, R., Wu, S.-Z., and Bezanilla, M. (2020). The Moss Physcomitrium (Physcomitrella) patens : A Model Organism for Non-Seed Plants. Plant Cell 32: 1361–1376.
Google Scholar: Author Only Title Only Author and Title

Robinson, D.G., Brandizzi, F., Hawes, C., and Nakano, A. (2015). Vesicles versus Tubes: Is Endoplasmic Reticulum-Golgi Transport in Plants Fundamentally Different from Other Eukaryotes? Plant Physiology 168: 393–406.
Google Scholar: Author Only Title Only Author and Title

Salama, N.R., Yeung, T., and Schekman, R.W. The Sec13p complex and reconstitution of vesicle budding from the ER with purified cytosolic proteins. The EMBO Journal 12: 4073–4082.
Google Scholar: Author Only Title Only Author and Title

Scheuring, D., Schöller, M., Kleine-Vehn, J., and Löfke, C. (2015). Vacuolar staining methods in plant cells. Methods Mol Biol 1242: 83–92.
Google Scholar: Author Only Title Only Author and Title

Schlacht, A. and Dacks, J.B. (2015). Unexpected Ancient Paralogs and an Evolutionary Model for the COPII Coat Complex. Genome Biology and Evolution 7: 1098–1109.

Google Scholar: Author Only Title Only Author and Title

Srivastava, R., Deng, Y., Shah, S., Rao, A.G., and Howell, S.H. (2013). BINDING PROTEIN Is a Master Regulator of the Endoplasmic Reticulum Stress Sensor/Transducer bZIP28 in Arabidopsis. Plant Cell 25: 1416–1429.
Google Scholar: Author Only Title Only Author and Title

Stagg, S.M., Gürkan, C., Fowler, D.M., LaPointe, P., Foss, T.R., Potter, C.S., Carragher, B., and Balch, W.E. (2006). Structure of the Sec13/31 COPII coat cage. Nature 439: 234–238.
Google Scholar: Author Only Title Only Author and Title

Stagg, S.M., LaPointe, P., Razvi, A., Gürkan, C., Potter, C.S., Carragher, B., and Balch, W.E. (2008). Structural Basis for Cargo Regulation of COPII Coat Assembly. Cell 134: 474–484.
Google Scholar: Author Only Title Only Author and Title

Takagi, J., Renna, L., Takahashi, H., Koumoto, Y., Tamura, K., Stefano, G., Fukao, Y., Kondo, M., Nishimura, M., Shimada, T., Brandizzi, F., and Hara-Nishimura, I. (2013). MAIGO5 Functions in Protein Export from Golgi-Associated Endoplasmic Reticulum Exit Sites in Arabidopsis. The Plant Cell 25: 4658–4675.
Google Scholar: Author Only Title Only Author and Title

Tanaka, Y., Nishimura, K., Kawamukai, M., Oshima, A., and Nakagawa, T. (2013). Redundant function of two Arabidopsis COPII components, AtSec24B and AtSec24C, is essential for male and female gametogenesis. Planta 238: 561–575.
Google Scholar: Author Only Title Only Author and Title

Vidali, L., Augustine, R.C., Kleinman, K.P., and Bezanilla, M. (2007). Profilin is essential for tip growth in the moss Physcomitrella patens. Plant Cell 19: 3705–3722.
Google Scholar: Author Only Title Only Author and Title

Vidali, L., van Gisbergen, P.A.C., Guérin, C., Franco, P., Li, M., Burkart, G.M., Augustine, R.C., Blanchoin, L., and Bezanilla, M. (2009). Rapid formin-mediated actin-filament elongation is essential for polarized plant cell growth. Proc. Natl. Acad. Sci. U.S.A. 106: 13341–13346.
Google Scholar: Author Only Title Only Author and Title

Viotti, C. et al. (2013). The Endoplasmic Reticulum Is the Main Membrane Source for Biogenesis of the Lytic Vacuole in Arabidopsis. Plant Cell 25: 3434–3449.
Google Scholar: Author Only Title Only Author and Title

Wang, X., Chung, K. P., Lin, W., and Jiang L. (2017). Protein secretion in plants: conventional and unconventional pathways and new techniques. Journal of Experimental Botany 69: 21-37.
Google Scholar: Author Only Title Only Author and Title

Whittle, J.R.R. and Schwartz, T.U. (2010). Structure of the Sec13–Sec16 edge element, a template for assembly of the COPII vesicle coat. The Journal of Cell Biology 190: 347–361.
Google Scholar: Author Only Title Only Author and Title

Wu, S.-Z. and Bezanilla, M. (2014). Myosin VIII associates with microtubule ends and together with actin plays a role in guiding plant cell division. eLife Sciences 3: e03498.
Google Scholar: Author Only Title Only Author and Title

Wu, S.-Z., Yamada, M., Mallett, D.R., and Bezanilla, M. (2018). Cytoskeletal discoveries in the plant lineage using the moss Physcomitrella patens. Biophys Rev 10: 1683–1693.
Google Scholar: Author Only Title Only Author and Title

Zeng, Y., Chung, K.P., Li, B., Lai, C.M., Lam, S.K., Wang, X., Cui, Y., Gao, C., Luo, M., Wong, K.-B., Schekman, R., and Jiang, L. (2015). Unique COPII component AtSar1a/AtSec23a pair is required for the distinct function of protein ER export in Arabidopsis thaliana. Proc Natl Acad Sci USA 112: 14360–14365.
Google Scholar: Author Only Title Only Author and Title

Zeng, Y., Li, B., Ji, C., Feng, L., Niu, F., Deng, C., Chen, S., Lin, Y., Cheung, K.C.P., Shen, J., Wong, K.-B., and Jiang, L. (2021). A unique AtSar1D-AtRabD2a nexus modulates autophagosome biogenesis in Arabidopsis thaliana. Proc Natl Acad Sci U S A 118.
Google Scholar: Author Only Title Only Author and Title

Zhang, H., Zhang, L., Gao, B., Fan, H., Jin, J., Botella, M.A., Jiang, L., and Lin, J. (2011). Golgi apparatus-localized synaptotagmin 2 is required for unconventional secretion in Arabidopsis. PLoS ONE 6: e26477.
Google Scholar: Author Only Title Only Author and Title